Passive acoustic quantification of gas fluxes during controlled gas release experiments

Benoît J. P. Bergès, Timothy G. Leighton, Paul R. White

Institute of Sound and Vibration Research

University of Southampton, Highfield, Southampton, Hampshire, UK

Corresponding author: Benoît J. P. Bergès, Institute of Sound and Vibration Research, University of Southampton, Highfield campus, Southampton, Hampshire, SO17 1BJ, UK

email: bjp.berges@soton.ac.uk

tel: (+44)2380 59 7153

Abstract

The detection and quantification of an underwater gas release is becoming increasingly important for oceanographic and industrial applications. Whilst the detection of each individual bubble injection events, with commensurate sizing from the natural frequency of the acoustic emission, has been common for decades in laboratory applications, it is impractical to do this when hundreds of bubbles are released simultaneously, as can occur with large methane seeps, or leaks from gas pipelines or undersea facilities for carbon capture and storage. This paper draws on data from two experimental studies and demonstrates the usefulness of passive acoustics to monitor gas leaks of this level. It firstly shows experimental validation tests of a recent model aimed at inverting the acoustic emissions of gas releases in a water tank. Different gas flow rates for two different nozzle types are estimated using this acoustic inversion and compared to measurements from a mass flow meter. The estimates are found to predict accurately volumes of released gas. Secondly, this paper demonstrates use of this method at sea in the framework of the QICS project (controlled release of CO_2 gas). The results in the form of gas flow rate estimates from bubbles are presented. These track, with good agreement, the injected gas and correlate within an order of magnitude with diver measurements. Data also suggest correlation with tidal effects with a decrease of 15.1 $\mathrm{kg\,d^{-1}}$ gas flow for every 1 metre increase in tidal height (equivalent to 5.9 L/min

when converted to standard ambient temperature [25 °C] and absolute pressure [100 kPa] conditions, SATP).

Keywords: carbon capture storage, methane seeps, inverse problem, passive acoustic, CO_2 release, leak monitoring

1 Introduction

The acoustic remote sensing of subsea gas leaks from anthropogenic and natural sources is becoming increasingly important. This applies not only to the detection of gas emissions (e.g. in order to alert pipeline users to a leak) but also its quantification in order to assess gas fluxes (e.g. in order to assess the growth rate of a leak and inform judgement of when to deploy costly intervention). Gas escaping underwater frequently takes the form of bubbles and leads to specific acoustic pressure fluctuations[1]. The size and structure of those releases vary from small bubble streams to larger bubble clouds and are potentially strong sources of sound.

There are several reasons for the increasing study of such releases, such as the need to better understand gas release mechanisms from natural sources, or the endeavor to put more control on leaks from industrial facilities. These are expanded on in the following.

Firstly as the oil and gas industry is facing increasing regulation with respect to marine environmental pollution, consequently there is a need for increased monitoring and control in the industrial processes[2,3]. Secondly concern regarding climate change has lead oceanographers to endeavour to better understand hydrocarbon gas releases as they play an important role in the carbon cycle[4,5]. Following several decades of interest in gas flux from the atmosphere into the upper ocean layer, and vice versa[6,7], in recent years there has been growing interest in the climate importance of gas flux into the ocean from the sediment. For example, long term monitoring of methane seepage in west Svalbard is needed to assess methane hydrate dissociation in this region[8]. Active acoustic techniques have frequently been used to locate and produce sonar images of, say, methane plumes[4]. In addition, sonar systems (e.g. scientific echosounders) hold the potential to produce quantification of gas flux[9–16]. For the purpose of long term monitoring (e.g. for early warning of leaks or monitoring of changes in leaks), the power requirement of a technology is critical. Active acoustic techniques tend to have higher power requirements[3] than passive acoustic systems, meaning that passive systems tend to be better suited to long term monitoring applications.

In the 1980s it was established that bubble size distributions and gas fluxes associated with natural processes could be quantified by identifying the natural frequency emitted by each gas bubble upon entrainment in the water[17], and this has subsequently been tested as a means for studying methane seeps[18–20]. However this technique can only be applied at flow rates that are sufficiently low to identify the acoustic 'signature' of each injection event. When the flow rate is high, the acoustic emissions of bubbles overlap and one is unable to distinguish individual bubble injection events[21]. Whilst signal processing methods (such as the Gabor transform[22,23]) can be helpful to isolate individual acoustic emissions from each bubble, they do not provide a complete solution. An alternative approach is needed to quantify high volumes of natural and industrial gas emissions. In industrial applications these are usually the releases which it is most imperative to correct, since they represent gas losses so great that they can lead to structural failure, as well as potential major economic and pollutionary impacts. Leighton and White[24] describe a scheme for quantifying the gas flux and bubble size distribution injected into liquid from high flux leaks. They test the applicability and robustness of their method against simulated data.

This work first tests the accuracy and applicability of the method[24] against experimental data. Clouds of bubbles were generated in a water tank using different bubble generation systems fed with nitrogen gas. The amount of gas injected in the system was controlled using a mass flow meter and the passive emissions were recorded with a calibrated hydrophone. Those results were processed and then compared to assess the accuracy in the various situations. This includes cases with constant or varying flow rates.

This quantification scheme is then used on data collected during the release phase of the QICS (Quantifying Impacts of Carbon Storage) project[25,26] that aimed at evaluating the impact of potential leaks from CCS (Carbon Capture and Storage) facilities. In May/June 2012, controlled CO_2 gas release was performed in Ardmucknish Bay (near Oban, west coast of Scotland). During this period, gas leaked from the seafloor in the form of bubbles and acoustic emissions were recorded using a hydrophone. The behaviour of the measured gas flux is investigated and compared with the amount of gas injected through the system and the tidal levels. The results are also compared to independent flow rate measurements from divers collecting gas directly from all the observed bubble streams.

2 Model

The method used in this study is aimed at determining bubble generation rate distributions from sound emissions from bubble plumes as proposed by Leighton and White[24]. Part of this theory will be outlined in this section to provide the background for the calculations that are presented in this study.

The starting point is the acoustic waveform received on a sensor which is close enough to a cloud of bubbles (whilst remaining in the acoustic far field) to record its emissions at an acceptable SNR (signal to noise ratio). The output of the inversion process is the bubble generation rates from which the gas flow rate (the experimental quantity measured here) is estimated.

As a bubble is released into the water column, it undergoes fluctuations in its volume which efficiently radiates sound[1]. These oscillations decay with time and so the detectable acoustic emission has a finite duration. The bubbles will be assumed to be spherical and volume changes result from oscillations of the bubble radius R about the equilibrium radius R_0. The oscillations occur close to the natural frequency of the bubble and decay exponentially. The natural frequency relates to the radius R_0 which has been used for decades to count and size bubbles in laboratories, and even in the natural world for studies of waterfalls[17], wave-breaking and rain at sea[27,22], and methane seeps[20]. When rapid gas releases occur, the bubble signatures overlap and the size distribution of the bubbles being produced can be characterized by the spectrum of the acoustic signal[28]. In obtaining absolute gas fluxes from such a spectrum, Leighton and White[24] suggest that the most important unknown is the acoustic energy released by an individual bubble. For want of a full description, a pragmatic solution can be adopted[24], specifically that each bubble is excited only once[21], generating an initial amplitude of bubble wall pulsation for the breathing mode ($R_{\epsilon 0\mathrm{i}}$), a quantity that, for want of further information[24], could be treated as being broadly invariant with depth and the nature of the gas-emitting orifice, an assumption that this paper will examine. Assumptions about the correct value of $R_{\epsilon 0\mathrm{i}}$ to use constitute the main source of uncertainty for the model and the estimated flow rates inferred using it. The parameter characterizing this effect in the model is the dimensionless ratio $R_{\epsilon 0\mathrm{i}}/R_0$. To date, only few studies provide measurements for this quantity[1,17,29–33]. In order to better predict this factor for different bubble sizes and nozzle types, more experimental and theoretical work is needed. For now, the most recent and complete estimate of this ratio comes from Deane and Stokes[33], who calculated $R_{\epsilon 0\mathrm{i}}/R_0$ for fragmented bubbles in sheared flow. Using these data (kindly provided by Grant Deane) and employing the assumption that $R_{\epsilon 0\mathrm{i}}/R_0$ is invariant with depth and bubble size, a confidence interval is determined based on the 25$^{\mathrm{th}}$ and 75$^{\mathrm{th}}$ percentiles of the Deane and Stokes data[33], respectively $R_{\epsilon 0\mathrm{i}}/R_0 = 1.4 \times 10^{-4}$ and $R_{\epsilon 0\mathrm{i}}/R_0 = 5.6 \times 10^{-4}$ (the fixed value of 3.7×10^{-4} used by Leighton and White[24] lies within this range). Moreover, calculation of the contribution of each bubble to the spectral magnitude of the acoustic emission at frequency f ($\omega = 2\pi f$) is[24]:

$$|X_{\mathrm{b}}(\omega, R_0)|^2 = \left[\omega_0 R_0^3 \frac{\rho_{\mathrm{w}} R_{\epsilon 0 \mathrm{i}}}{r R_0}\right]^2 \frac{4\left[(\omega_0 \delta_{\mathrm{tot}})^2 + 4\omega^2\right]}{\left[(\delta_{\mathrm{tot}}\omega_0)^2 + 4(\omega_0 - \omega)^2\right]\left[(\delta_{\mathrm{tot}}\omega_0)^2 + 4(\omega_0 + \omega)^2\right]}, \quad (1)$$

where r defines the distance from the hydrophone to the bubble cloud, ρ_{w} the water density and ω_0 is the angular natural frequency of the gas bubble[1]. Eq. (1) is derived analytically by Leighton and White[24] by taking the Fourier transform of the temporal pressure fluctuations of a gas bubble after injection. The dimensionless damping factor δ_{tot} is calculated using the revisited bubble damping theory[34,35] and Prosperetti theory[36,37]. The angular natural frequency ω_0 can be expressed as[1]:

$$\omega_0 = \frac{1}{R_0\sqrt{\rho_{\mathrm{w}}}}\sqrt{3\kappa\left(p_0 - p_{\mathrm{v}} + \frac{2\sigma}{R_0}\right) - \frac{2\sigma}{R_0} + p_{\mathrm{v}} - \frac{\eta_{\mathrm{S}}^2}{\rho_{\mathrm{w}} R_0^2}}, \quad (2)$$

with κ the ratio of specific heats and p_0 the hydrostatic pressure. This formula accounts for the effects of vapour pressure p_{v}, surface tension σ and shear viscosity η_{S}. It should be noted that κ and δ_{tot} are dependent on the composition of the gas inside the bubble.

If it is assumed that the acoustic emissions of each bubble are uncorrelated, the power spectral density $S(\omega)$ of the the acoustic signature of the leak is given by:

$$S(\omega) = \int_0^{\infty} D(R_0)\, |X_{\mathrm{b}}(\omega, R_0)|^2 \, dR_0, \quad (3)$$

with $D(R_0)$ defining the rate at which bubbles of radius R_0 are generated. Eq. (3) defines a Fredholm integral equation of the first kind that can be approximated at discrete frequencies ω_l, $l = 1, \ldots, N_\omega$ and bubble radii R_n, $n = 1, \ldots, N_R$:

$$S(\omega_l) \approx \sum_{n=1}^{N_R} \psi(n) \left|X_\mathrm{b}(\omega_l, R_n)\right|^2 \Delta R_n, \tag{4}$$

with ΔR_n the bin width for the n^{th} radius bin. Here, the center of the radius bins are taken to be equally spaced and the bin width is therefore constant, $\Delta R_n = \Delta R_0$. The quantity $\psi(n)$ represents the bubble generation rate within a radius bin in number of bubbles $\mu\mathrm{m}^{-1}\mathrm{s}^{-1}$ (where the $\mu\mathrm{m}^{-1}$ represents the fact that a bubble generation rate is determined for each bubble radius size bin, which by convention is of one micron width). For the set of frequencies and bubble radii, Eq. (4) can be expressed in matrix form:

$$\mathbf{S} = \Sigma\Psi, \tag{5}$$

with $\mathbf{S}$ and Ψ the column vectors containing respectively the elements $S(\omega_l)$ and $\psi(n)$. The spectral matrix Σ is constructed at each ω_l and R_n using Eq. (1), $\Sigma_{l,n} = \left|X_\mathrm{b}(\omega_l, R_n)\right|^2 \Delta R_0$ and is of size $N_R \times N_\omega$. In Eq. (4), Ψ is to be estimated through solving the inverse problem $\Psi = \Sigma^{-1}\mathbf{S}$. Techniques to solve problems in this form are for example detailled by Hansen[38,39]. If the number of radius bins N_R and the number of frequencies N_ω are chosen to be equal, the spectral matrix Σ is square, which mitigates against potential over-or under-determination of the problem. The problem tends to be ill-conditioned and the inevitable measurement errors in $\mathbf{S}$ lead to large errors in the estimated bubble generation rates. To mitigate this, it is prudent to include some form of regularization. In this paper, Tikhonov regularization is used[39]:

$$\Psi_\alpha = \left(\Sigma^t\Sigma + \alpha^2\mathbf{I}\right)^{-1}\Sigma^t\mathbf{S}. \tag{6}$$

For the choice of the regularization factor α, the Generalized Cross Validation (GCV) criterion function $H(\alpha)$ is computed. For Tikhonov regularization, the GCV criterion can be expressed as[39]:

$$H(\alpha) = \frac{\|\Sigma\Psi_\alpha - \mathbf{S}\|_2^2}{\left(N_\mathrm{b} - \mathrm{tr}\left(\left(\Sigma^\mathrm{t}\Sigma + \alpha^2\mathbf{I}\right)^{-1}\Sigma^\mathrm{t}\right)\right)}, \tag{7}$$

and α is chosen so that $H(\alpha)$ is minimized and fulfils a positivity constraint for the bubble generation rate distributions $\psi_\alpha(n) > 0, \forall\, n$. From this and assuming spherical bubbles, the flow rate is estimated using:

$$F_\mathrm{g} = \frac{4\pi}{3}\sum_{n=1}^{N_R}\psi_\alpha(n)\, R_\mathrm{n}^3\Delta R_0. \tag{8}$$

Leighton and White[24] outline key simplifications that they note require further research, such as the assumption that each bubble rings only once (when of course subsequent fragmentation of that bubble would cause subsequent emissions) and that the excitation $R_{\epsilon 0\mathrm{i}}/R_0$

is simplified to an expression which ignores details of the way the gas is released (through nozzle, pipe rupture, seabed seepage etc.) and the mechanisms of excitation[40–42], when even reshaping or reorientation of a given nozzle can in some circumstances change the acoustic emission. Therefore it was important to undertake a validation exercise to investigate to what extent the inversion scheme described here allows useful gas flux estimates to be made before the developing theoretical basis for bubble excitation mechanics can progress to a level to use in this model.

3 Experimental procedure

A Test tank experiment

Measurements of passive acoustic emissions of bubble clouds were conducted in a 8 m x 8 m x 5 m deep (i.e. of volume $V = 320\ \mathrm{m}^3$) test tank containing fresh water at $10\,^{\circ}\mathrm{C}$ (Fig. 1). A schematic of the experimental procedure is presented in Fig. 1(a). Two bubble generation systems were used: a commercial bubbling stone designed for aquarium use (Fig. 1(b)); a needle array consisting of six needles with a nozzle inner diameter of 1 mm arranged in circle with a spacing of approximately 3 cm on a flat platform (Fig. 1(c)). A nitrogen gas cylinder was used to produce the gas for generating the bubbles. The outflow of the bottle was connected to a mass flow meter (Bronkhorst high-tech in-flow F-111BI) to adjust the volumetric flow rate along with a data acquisition unit. One or the other of the two bubble generation systems were then connected to the end of the gas line and deployed at the bottom of the test tank. Acoustic pressure was recorded using a hydrophone (bandwidth of 2 Hz - 48 kHz, sensitivity of -165 dB re 1 V/μPa). First, 30 seconds of continuous acoustic measurements of bubble emissions at different regimes (flow rate kept steady during the 30 seconds, 15 regimes) were performed at a sample rate of 48 kHz. The 15 regimes are from $0.1\,\mathrm{kg\,d^{-1}}$ to $3\,\mathrm{kg\,d^{-1}}$, equivalent to 0.1 to 3.7 L/min SATP[a]. As a second test, gas flow rate was varied manually and monitored (from $0.1\,\mathrm{kg\,d^{-1}}$ to $3.8\,\mathrm{kg\,d^{-1}}$, equivalent to 0.1 to 4.7 L/min SATP) for 200 seconds. The acoustic signals were acquired. This test was also conducted for both of the two bubble generation systems. In addition, measurements of the ambient noise were performed in order to study impact on the estimated gas fluxes.

For the acquisition of the acoustic signals, a wildlife acoustic SM2M+ recorder was used. This consists of a buoyant body containing an acquisition board powered by internal battery connected to a calibrated hydrophone. The unit was loaded on the bottom of the test tank. Whilst use of a hydrophone array would have produced benefits in terms of gain and directionality[24], this experiment was designed to test the lowest cost (single hydrophone) option, and was appropriate for this short range tank test. Also, this allowed the testing of the experimental set-up used for the field measurements (Sec. 3 B).

In order to collect measurements relating to the free field, it was important to take

[a] Throughout this paper, flow rates are given as mass flow rates (expressed in kg $\mathrm{d^{-1}}$), quantities that are independent of ambient temperature and absolute pressure conditions and gas composition. In the text (but not the figures) there is space to add, in addition, what these flow rates would be when converted to Standard Ambient Temperature and Pressure (SATP, temperature of 25 °C and absolute pressure of 100 kPa). For clarity, all SATP conversions will be stated in L/min.

into account the effect reverberation has on the recorded signals. For this purpose, care was given to position the hydrophone close to the bubble release, where the direct field dominates over the reverberant field. In order to evaluate this effect, the radius of reverberation r_0 is introduced. This is defined as the distance from the source where the direct and reverberant fields have equal contribution[43,44] $r_0 = \sqrt{AQ_\theta/16\pi}$ with $A = 55.3 \times \dfrac{V}{T_{60}c}$ the Sabine coefficient being dependent on the volume of the enclosure V, the speed of sound in the medium c and the reverberation time T_{60} of the enclosure. The quantity Q_θ is the directivity factor, equal to 2 for an omnidirectional source sitting on a reflective flat surface[43]. For the enclosure used in this experiment, $T_{60} = 181\,\mathrm{ms}$ between 0.8 kHz and 8 kHz, giving $r_0 = 1.62\,\mathrm{m}$. The distance from the bubbles to the hydrophone was of 1 m. At this range, the total acoustic field is 5.6 dB higher than the reverberant field and the direct field is determined within 1.4 dB. Another important limitation on the measurement in a reverberant enclosure is the mode mixing, i.e. working at frequencies where there is enough modal overlap to give an acoustic field that is isotropic and homogeneous. This condition can be fulfilled by working at frequencies higher than the Schroeder frequency[43] $f_{\min} = c \times \sqrt{6/A}$. In this study this gives $f_{\min} = 447\,\mathrm{Hz}$ which is well below the minimum frequency of interest (796.8 Hz, corresponding to the highest bubble size considered). Also, care was given at placing the bubble injection site (after the method of Leighton et al.[45]) in order to reduce the driving effect of the bubble emissions on the bubble itself, after reflection from the tank walls, to a level that did not significantly change the bubble natural frequency[46] and damping[45] within the experimental uncertainty, and so no corrections were necessary for these effects (quantitative assessments of these corrections should be considered when taking such data in reverberant test tanks).

In order to determine gas flow rates, the model described in Sec. 2 is applied to the hydrophone measurements through Eq. (6) with the range $r = 1$ m and the regularization factor α determined through Eq. (7). This results in bubble generation rate distributions Ψ that are further converted into volumetric flow rates (Eq. (8)). Volumetric to mass flow rate conversion is performed for measurements of the mass flow meter and acoustically-inferred flow rates based on the ideal gas law (accounting for the ambient temperature of 10 °C, absolute pressure conditions at 5 m depth, and gas composition). Bubble sizes are chosen to be from $R_0 = 0.5$ mm to $R_0 = 5$ mm, with 50 linearly spaced bins. The choice of the bubble radius range is dictated by the need to have Ψ decreasing at the largest bubble radii. For each radius bin R_n is associated a natural frequency ω_0, calculated using Eq. (2). So for example, at $R_n = 0.5$ mm and $R_n = 5$ mm, $\omega_0 = 796.8$ Hz and $\omega_0 = 7973.3$ Hz respectively. In this frequency range, the spectrum $\mathbf{S}$ is first computed from the time series in 154 linearly spaced frequency bins. Interpolation of $\mathbf{S}$ at the 50 frequencies corresponding to ω_0 is then performed prior to the inversion process. Furthermore, because the model is dependent upon the factor $R_{\epsilon 0 \mathrm{i}}/R_0$ that remains a source of uncertainty, a confidence interval is given based on the data from Deane and Stokes[33]. This factor is taken to be invariant with depth and bubble radius, and in the bubble range of interest, a statistical analysis of these data (871 bubble emissions of bubbles from 0.5 mm to 2.6 mm) gives $R_{\epsilon 0\mathrm{i}}/R_0 = 5.6 \times 10^{-4}$ for the 75$^{\mathrm{th}}$ percentile and $R_{\epsilon 0\mathrm{i}}/R_0 = 1.4 \times 10^{-4}$ for the 25$^{\mathrm{th}}$ percentile. Because the model is scaled by the quantity $\left(\omega_0 R_0^3 \frac{\rho_\mathrm{w} R_{\epsilon 0\mathrm{i}}}{r R_0}\right)^2$ and Ψ is obtained as the inverse of the spectral matrix Σ, the low solution bounds correspond to the 75$^{\mathrm{th}}$ percentile while the high bounds of the estimates are computed using the 25$^{\mathrm{th}}$ percentile.

For the case of steady flow rates, power spectral densities are calculated from 30 second acoustic recordings for each regime. Prior to inversion the spectrum of the recorded ambient noise is subtracted to isolate the contribution of the bubbles. The SNR is computed by forming the ratio of a bubble sound spectrum to the ambient noise spectrum. For the processing of the 200 second varying flow rates, a spectrum is computed each second. For each spectrum, the inversion scheme is applied and the released gas volume can be estimated and the fluctuations tracked.

B QICS experiment

The release phase of the QICS project[25,26] (aimed at investigating potential impact of gas leakage from geological carbon storage) was conducted from 17$^{\mathrm{th}}$ of May to 22$^{\mathrm{nd}}$ June 2012. Throughout this period, CO_2 gas was released from a diffuser under the seabed at a controlled rate. Taylor et al.[47] describe the set-up of this large scale experiment and outcomes of this project are discussed by Blackford et al.[26]. Here, gas escaping the seafloor that took the form of bubbles in the water column is investigated. Gas in sub-surface sediments is investigated and discussed in Cevatoglu et al.[48]. On 13rd June, a SM2M+ recorder (wildlife acoustics) was deployed using a mooring and was positioned approximately 1 m from the seafloor. The unit was moved on 15th June by divers into the region where bubble releases occurred. The depth of the region where the bubbles escaped varied with tide and was of 10-12 m. The gas injection was stopped on 22nd June, thus there was a period of 7 days during which acoustic signals were acquired and gas was being injected. The hydrophone unit was recovered on 29th June. The recorder measured continuously during this period at a sample rate of 48 kHz. The inversion scheme is to be applied to the data, following the method described in Sec. 3 B.

From the acoustic time series, a spectrum **S** for each 10 second segment of data is computed and constitutes the input to the inversion. A spectrogram of the data 15th to 26th June is presented in Fig. 2, with periods with (15th to the end of 22nd June) and without (end 22nd to 26th June) bubble emissions. Also, acoustic energy from three seal deterrent devices (sdd) can be observed from 15th to the end of 20th June. These are identified as Airmar dB Plus II sited at 2 fish farms ≈ 5 km and ≈ 6.5 km from the gas release site and emitted continuously until the 20th where they were turned off for 5 days. A closer analysis of the acoustic signature is presented in Fig. 3(a) (spectrogram over 60 seconds on 25th June, gas injection stopped, no acoustic emission from gas bubbles). It shows the combination of the three sdds with the continuous emission of sound pulses. Most of the acoustic energy is concentrated around the 10 kHz frequency band. This is consistent with the results from

Gordon and Northridge[49], showing that this device affects a frequency range between 5 kHz and 15 kHz. Fig. 3(b) illustrates this by comparing the ambient noise spectrum with and without the devices on. The signals analysed here are those measured after the gas injection was stopped and they do not contain the acoustic emission of bubbles. Whilst at low frequencies (< 2 kHz) the two spectra are close, at higher frequencies they diverge with a maximum difference of approximately 32 dB at 10 kHz. The passive acoustic inversion should be applied on the spectral contribution only from the bubbles (otherwise, the bubble count can be artificially inflated). To that purpose, two steady noise floor spectra when there was no acoustic emissions from bubbles are computed from 3 minutes of data collected on 24$^{\text{th}}$ June (no noise from sdd) and on 25$^{\text{th}}$ June (sdd turned on). As in Sec. 3 A, these spectra are then used to subtract steady ambient noise.

The ambient noise level varies during the experiment as a function of time. This was in part the result of the passage of vessels near the site and activity associated with the experiment. To reduce the impact of transient noise events and to smooth the results somewhat, the results from each 10 s sequence were combined using a 1 hour rolling median filter. Noise sources which persisted for more than 30 minutes would inevitably corrupt the bubble estimates artificially by inflating the bubble count. Such an event happened at the time at which the divers measured the gas flux or toward the end of the experiment, and the implications of this will be discussed in Sec. 4 C.

For the inversion, 50 bubble radius bins linearly spaced from 0.5 mm to 10 mm are chosen in order to have Ψ decreasing at the largest bubble radii. The spectra $\mathbf{S}$ are first interpolated at the corresponding frequencies (from 451 Hz to 9034 Hz) using Eq. (2). The inversion is carried out as described in Sec. 3 A. However, because there were multiple bubble streams (contrary to the test tank experiment where bubbles were release from a single location), a critical variable to evaluate is the range r because Eq. (1) is proportional to $1/r^2$.

If one assumes that the leak comprises N_s sources of the same size located at ranges r_m, $m = 1, \ldots, N_\mathrm{s}$, one can consider an equivalent leak from a single source. The flux of this single leak is then the sum of all the smaller sources, but is located at an 'effective' range, r_eff, where $1/r_\mathrm{eff}^2 = \sum_{m=1}^{N_\mathrm{s}} 1/r_m^2$. Each range r_m was determined from pockmarks revealed by multi-beam echosounder mapping on the morning of 20$^{\mathrm{th}}$ June (corresponding to low tide). This is shown in Fig. 4 with the location of the pockmarks, the diffuser and the hydrophone indicated. This only constitutes a snapshot at a specific point in time. Evaluating the range r_eff from this image does not take into account potential appearance or disappearance of bubble streams throughout the measurement period. While ideally one would determine the location and appearance of each release, the position taken here of assuming a single effective range is constrained by technical limitations. This issue could be mitigated by the use of an array of hydrophones instead of a single sensor in order to locate and monitor each stream of bubbles. Alternatively, if resources allowed it, a dedicated camera or active sonar systems could be used to identify where and when the gas releases occurred in order to provide these data as input for the passive sonar study. Using the map presented in Fig. 4, 57 pockmarks are identified and from the location of the hydrophone, it is found that distances from bubble streams to the acoustic sensor vary from 0.8 m to 6.5 m. The resulting effective range is $r_{\text{eff}} = 2.4$ m to input in Eq. (1). Similarly to Sec. 3 A, results are given in the form of a confidence interval based on the data from Deane and Stokes[33].

4 Results and discussion

A Overview of results

Preliminary validation tests were conducted in a water-filled tank (Fig. 5-9), as a precursor to the at-sea QICS measurements (Fig. 10-13). Before discussing both in detail, it is useful to understand where these tests are leading, as this explains the accuracy, uncertainty, and advantages of the passive acoustic technique. Consider the lower plot in Fig. 11, which shows the mass flux at QICS as inferred from the passive acoustic emissions. The results are presented as a range of acoustic estimates based on the amplitude of the initial excitation $R_{\epsilon 0\text{i}}/R_0$ (Sec. 3 A). In future, the developing theoretical basis should allow $R_{\epsilon 0\text{i}}/R_0$ to be refined for different type of injection (e.g. from a needle, a leaking gas pipe, or the seabed), which may well reduced the uncertainty associated with the method used in this paper.

Half way through 19$^{\text{th}}$ June, a single cross overlies the lower curve in Fig. 11. This is the gas flux measurements made at a single point in time by divers on each visible bubble stream using an inverse funnel. It lies well within the borders of the acoustically-inferred gas flux, adding confidence to the latter. However, as explained in Sec. 3 B, the acoustic signal here is contaminated by noise from the boat and divers, and so a more realistic comparison is to compare the diver-generated flux estimate with the acoustically-inferred fluxes at similar points in the tidal cycle either side of the diver measurement. One further point from the comparison of diver- and acoustically-generated fluxes is this: it illustrates the power of the passive acoustical method. Whilst the divers, at considerable expense and effort, managed to obtain only one data point for the gas flux, the passive acoustic method monitors the gas flux in real time, continuously, over 7 days. For example, over the whole bubble release field, it details the temporal correlation of the gas flux with the tidal cycle (as shown on Fig. 11-13).

Having therefore provided perspective to the data to be presented in this section, the results from laboratory trials (Sec. 3 A) are discussed with the assessment of the accuracy of the technique in a controlled environment in Sec. 4 B. Sec. 4 C then presents the results from the passive acoustic data collected at sea during the QICS experiment.

B Test tank results

B.1 Inversion process considerations

Under laboratory conditions, the experimental assessment of the model is performed by comparing the flow rates inferred from acoustics to the measurements from the mass flow meter. This is repeated for 30 different scenarios, specifically 15 flow regimes (mass flow rates from $0.1\,\mathrm{kg\,d^{-1}}$ to $3\,\mathrm{kg\,d^{-1}}$, equivalent to 0.1 to 3.7 L/min SATP, as shown in Table 1), for each of the two bubble injection systems. Scenarios with varying flow rates over a 200 seconds time period are also carried out.

The passive inversion process described in Sec. 2 is based on the spectrum of the signals emitted from bubbles as measured by a calibrated hydrophone in the tank. The signals consist of 30 seconds of data at a constant flow rate. Examination of the time series are shown in Fig. 5(b) and Fig. 5(c) and reveals single bubble signatures are indistinguishable because the signals from different bubbles are heavily overlapped. Also, an increase in acoustic pressure amplitude with increasing flow rates can be observed. Fig. 5(a) presents the power spectral densities from signals recorded at a range of 1 m, distance where the direct field is dominant (Sec. 3 A). Spectra for the ambient noise and the signals emitted by the two bubbling systems in regime 15 (which has the highest flow rate - Table 1) are presented. For the inversions, the radius range used is 0.5 to 5 mm which, using the inverse of Eq. (2), approximately corresponds to the frequency band 0.8 to 8 kHz, fulfilling the condition for the minimum frequency to be used in the enclosure $f_{\mathrm{min}} = 447\,\mathrm{Hz}$. In this band, the noise floor presents a spectral level equivalent to an acoustic noise between $55.5\,\mathrm{dB\,re\,1\mu Pa^2\,Hz^{-1}}$ at 0.9 kHz and $45.6\,\mathrm{dB\,re\,1\mu Pa^2\,Hz^{-1}}$ at 7.2 kHz. The sound associated with bubble generation is from 3 dB at the highest frequency of interest to 18 dB (at lower frequencies) greater than the ambient noise. The noise spectrum is subtracted from the signal spectrum to avoid the artificial enhancement of the bubble count[50] even though within the analysis band, the signal from the bubble generation process remains greater than the noise floor. In cases where the measured spectrum is close to the noise spectrum, limited information about the bubble generation is available. The processing methodology adopted here is based on a fixed bandwidth and the band where noise dominates are assumed to have zero contribution from the bubble generation process. Such an assumption is inconsistent with any solution for a strictly positive bubble generation rate, since bubbles of any size make some contribution to all frequencies, as $|X_{\mathrm{b}}(\omega, R_0)|^2 > 0$ for nearly all combinations of ω and R_0. This theoretical issue is relieved by the use of regularization. However as the flow rate is reduced the frequency bands where the noise dominates become more prevalent, so the accuracy of the estimation reduces as the need for regularization increases.

Fig. 6 depicts the rate of generation of bubbles, per micron radius increment Ψ calculated using Eq. (6) (Fig. 6(a)) with help of the GCV function $H(\alpha)$ (Fig. 6(b)). The low frequency components are greater for the arrangement of needles (Fig. 5(a), f <2 kHz), this translates to a higher bubble count at large bubble radii. Whereas the greater energy in the high frequency band of the bubbling stone spectrum (Fig. 5(a), 4 kHz to 6 kHz) results in Ψ exhibiting larger levels at low bubble radii (e.g. at $R_0 < 1$ in Fig. 6(a)). Trends in bubble size distributions can be inferred from the inversion results, and those from all the regimes (e.g. by fitting power laws to the various regimes and bubblers) but rather than doing so it would be better to question first the reliability of perceived details and differences from such an inversion.

For each given flow regime, the acoustically-estimated bubble generation rate is integrated across all bubble sizes to obtain the estimated flow rate. This is then compared with the metered value (Table 1). Thus, since each regime/bubbler combination gives a single data point, all these combinations can be plotted and compared (Fig. 7(a) and (b), left axis). SNR is also presented (Fig. 7(a) and (b), right axis) and it can be observed that the accuracy of the model is dependent on the regime. The error bars represent the uncertainty in the estimated gas flux from statistical analysis on the data from Deane and Stokes[33] as described in Sec. 3 A. Although the confidence interval inferred this way spans 12.2 dB, this will reduce as theoretical and experimental studies on the initial amplitude of bubble wall pulsation for the breathing mode ($R_{\epsilon 0 \mathrm{i}}$) develop. Here, the relative change in flow rate compared to metered gas volumes is of interest. This would demonstrate the ability of the inversion technique to accurately predict temporal changes in flow rates.

B.2 Steady flow rates

From Fig. 7(a) and (b), the relative change in flow rate for the highest regimes is predicted with good agreement from the acoustics, this for both bubble generation systems. The change in flow rate is then resolved without significant impact from the factor $R_{\epsilon 0 \mathrm{i}}/R_0$ at the highest flow rates (15 to 5). However, at the smallest flow rates (5 to 1), when the SNR is poorer (Fig. 7, right axis), the acoustic inversion fails to follow the metered reduction in flow rate, as expected because here the noise significantly corrupts the measurements and lessens the ability to infer flow rate. The model considered is able to monitor temporal variations in gas volume released with a good precision, given the SNR is sufficient. At lower flow rates, the error becomes significant and sizing each bubble from the natural frequency[18,20] might be more suited if single bubble signatures can be identified. It should be added that a single hydrophone is used in this study and the SNR could be increased with the use of an array of sensors.

This analysis assumes $R_{\epsilon 0\mathrm{i}}/R_0$ is constant, this quantity affects the accuracy of the estimates for each regime. By matching the acoustic estimates on the mass flow meter measurements allows to evaluate $R_{\epsilon 0\mathrm{i}}/R_0$ for the different nozzle type and regimes (Table 1). The needle array results in values of $R_{\epsilon 0\mathrm{i}}/R_0$ between 2×10^{-4} and 3.3×10^{-4} for regimes 15 to 5 (range of regimes where the SNR is best). In these regimes, the bubbling stone estimates results in values of $R_{\epsilon 0\mathrm{i}}/R_0$ between 1.4×10^{-4} and 1.9×10^{-4}. These values all lie within the 25$^{\mathrm{th}}$ and 75$^{\mathrm{th}}$ percentiles of the considered data set[33] for $R_{\epsilon 0\mathrm{i}}/R_0$.

B.3 Varying flow rates

In order to assess further the applicability of the technique it is tested with a flow rate varying over a period of 200 seconds for both the needle array and bubbling stone. Direct comparison of the computed flow rates from acoustics is given through a confidence interval based on the uncertainty on $R_{\epsilon 0\mathrm{i}}/R_0$ (Sec. 3 A). The results are shown in Fig. 8(a) and (b).

In both figures, the metered flow rates lie within the confidence interval. In addition, the changes in gas injection is accurately tracked by the acoustically-inferred flow rates. Also, it can be observed that the estimates can fluctuate locally due to the influence of noise. This issue can be mitigated with the use of a filter to smooth the final results.

The different calculation stages for the inversion scheme applied to these data are presented in Fig. 9. Each step for the varying flow rate on a period of 200 seconds is shown for the case of the needle array (Fig. 9(a), (c), (e)) and the bubbling stone (Fig. 9(b), (d), (f)). This includes the spectrogram of the data to be inverted (Fig. 9(a), (b)), the resulting bubble generation rate distributions Ψ (Fig. 9(c), (d)) and finally the mass flow rates (Fig. 9(e), (f)). Just as was done for the steady flow rate data of the preceding section, $R_{\epsilon 0\mathrm{i}}/R_0$ are estimated and presented in Fig. 9(e) and (f) (right axis). An optimized value is then used to compute an estimate that best fits the metered flow rates. This gives $R_{\epsilon 0\mathrm{i}}/R_0 = 3.5 \times 10^{-4}$ for the needle array and $R_{\epsilon 0\mathrm{i}}/R_0 = 1.6 \times 10^{-4}$ for the bubbling stone. The optimized flow rates solution is obtained by averaging the values of $R_{\epsilon 0\mathrm{i}}/R_0$ presented in Fig. 9(e) and (f) (left axis). When comparing the spectrum with Ψ, correlation can be observed with dominant spectrum level at low frequencies resulting in a high bubble count at large bubble radius. Moreover, the largest bubbles contribute most to the computed flow rates. If the optimized values of $R_{\epsilon 0\mathrm{i}}/R_0 = 3.5 \times 10^{-4}$ for the needle array and $R_{\epsilon 0\mathrm{i}}/R_0 = 1.6 \times 10^{-4}$ for the bubbling stone are used, an estimation for the total amount of gas released (mass in kg) can be computed from passive acoustics. Then, the accuracy of the inversion over the 200 seconds can be addressed by comparing these results to the measurements from the mass flow meter. For the scenario presented in Fig. 9(e) (needle array), 4.8×10^{-3} kg of nitrogen is released over 200 seconds and the acoustic inversion estimates 5.2×10^{-3} kg, over estimating the metered amount by 10%. In the case of the bubbling stone (Fig. 9(f)), the estimation of 5×10^{-3} kg is to be compared to 5.1×10^{-3} kg measured from the mass flow meter, giving an underestimation of 4%.

Results from both trials clearly show that the inversion scheme can detect temporal changes and demonstrate the ability of the technique to characterize gas leaks precisely. In practical uses for today's industrial leaks (in order to assess of gas leaks levels for oil and gas facilities) or high volume methane seeps (to investigate temporal variability over long periods of time), estimates of gas flux to within an order of magnitude are usually useful. Better characterization of emission mechanisms[33,40,41] will improve the accuracy of the method in line with the deployment of new methods for increasingly accurate estimates of the void fraction of gas bubbles beneath the seabed[51–53].

C QICS results

C.1 Inversion process considerations

Through the release phase of the QICS experiment, passive acoustic emission from bubble releases were recorded for 7 days, from 15th to 22nd June. Using the inversion scheme gas flow rates are estimated (Sec. 3 B). Results are investigated in order to determine the applicability of the passive acoustic inversion method in an at sea environment. The procedure is similar to the one used for the test tank experiments with varying flow rates. Spectra that are determined for every 10 seconds of signals constitute the input of the model. Inversion is applied similarly. As observed in Sec. 4 B, the inversion scheme is sensitive to noise, especially for the set-up considered here with a single hydrophone. Various sources of noise disturbed the measurements and contribution of noise sources such as seal scrammers could be mitigated (Sec. 3 B, Fig. 3) by subtracting its contribution to the inverted spectrum. However, noise events such as those arising from boat activities could not be accounted for, resulting in mass flow rates varying significantly. This is observable in Fig. 10 (solid grey line) where occasional large spikes in the estimated flow rate are evident. In order to reduce the effect of these random noise events, the 1 hour median filter is applied, resulting in a smoothed solution (Fig. 10, solid black line), reducing artificial local fluctuations.

The resulting flow rates are presented in the form of a confidence interval (Sec. 3 A) and are to be compared with injected flow rates. The results (from 15^{th} to 23^{rd} June) are presented in Fig. 11 with bubble generation rate distributions Ψ (Fig. 11(a)), tide levels (Fig. 11(b)), injected and acoustically-inferred flow rates (Fig. 11(c)). Even though a median filter is applied to the data as in Fig. 10, strong fluctuations in flow rates can be observed (e.g. around 20^{th} 12.00 am, 21^{st} 12:00 am and 22^{nd} June after mid-day). This corresponds to increased boat activity around the experimental site and results in artificially increased bubble count (thus producing overestimated mass flow rates). A similar increase in flow rate estimates can be observed on 19th June 12:00, time where divers undertook flow rate measurements near the hydrophone. This effect cannot be fully corrected by the use of the 1 hour median filter.

C.2 Correlation with tidal heights

A strong correlation of the estimates from the acoustic measurements with the tidal height can be seen in Fig. 11, a correlation also noted in the time lapse photography and pCO_2 data[26]. This variability with changing hydrostatic pressure is noteworthy and diverse for marine seeps[12,54–60]. Here, the variability with tidal height is noticeable in the bubble generation rate distributions Ψ (Fig. 11(a)) and in estimated flow rates (Fig. 11(c)). Using a 12 hour Hamming window with 50% overlap, the cross power spectral density between the upper bound of the estimated flow rates and tidal heights is computed (Fig. 12(a)). This exhibits peaks at diurnal (24 hour period) and semi-diurnal cycles (12 hour period). Here, the tidal height is dominated by the semi-diurnal component. From the Fourier transforms of the tidal heights and the flow rates over windows of 12 hours with 50% overlap from 14^{th} 05:30 pm to 22^{nd} 02.00 pm, 29 phase delays for the semi-diurnal cycle at different times are calculated. The histogram of these estimates is shown in Fig. 12(b) and it indicates a delay of $174° \pm 23°$ (5.8 ± 0.8 hours) between tidal heights and flow rates. The point where the release of gas is highest is then located just before the lowest level of tide and low hydrostatic pressure corresponds to high levels of gas release while high pressure corresponds to low flow rates.

Various authors[12,55–60] have noted a range of relationships between their measures of gas flux and tidal cycle in natural seeps, though no statistical analysis of the correlation (as done above) has previously been undertaken. The results from earlier authors range greatly. For natural seeps at a depth of 70 m, using a single frequency active sonar, Schneider von Deimling et al.[12] reported that the greatest flux follows high tide after a 90° phase delay, which Leifer and Boles[54] suggest could be due to effects associated with the diffusion of gas in the sediments. Conversely, for natural seeps at a depth of 67 m, using seep tents, Boles et al.[60] reported that greatest gas fluxes occurred at low tide, which they attributed to the activation/de-activation of individual seeps. This variation is perhaps not unexpected given the variation in ocean depth and injection conditions, but furthermore the limitation of the different measurement techniques must be recalled. In a noise-free environment, the passive acoustic technique will accurately record the bubble volume if the initial excitation amplitude ($R_{\epsilon 0\mathrm{i}}/R_0$) and distance to the leak are known, but noise degrades the accuracy. If single frequency active acoustic techniques are used, it must be recalled that there is an inherent ambiguity between the number of large bubbles, and the number of resonant bubbles which is not resolved unless a full inversion is done[61] or a nonlinear method is employed[62]. In the absence of such an inversion, an increase in the signal from a single frequency sonar could represent an increase either in the number of bubbles that are of resonant size, or in the number of large bubbles. Furthermore, any such inversion must take account of the variations from standard bubble resonance theory if the bubble size is not much smaller than a wavelength[34,35].

In order to further characterise the relation between the tide and the ebullition rate, Fig. 13 presents tide plotted against the upper bound of the estimated flow rates. Tidal height is sampled every 43 minutes and flow rates are averaged between two data points. The tidal effect is investigated from 14th 05:30 pm to 18th 02.00 pm, period during which the noise is limited. Fig. 13(a) shows results for each tidal height data point together with a linear regression with a regression coefficient of $R^2 = 0.7$. Refining the focus to peak tide changes with flow rates averaged over 86 minutes around tidal height peaks and dips gives a linear regression to the subsequent 13 data points with a regression coefficient of $R^2 = 0.9$. This increased correlation between tidal height and flow rate suggests that the change in flow rates is more closely related when the tidal cycle is at its local maximum or minimum[60]. Results suggest a decrease of 15.1 kg d^{-1} (5.9 L/min SATP) for each meter increase in tide around tidal height peaks.

C.3 Comparison with gas injection and diver measurements

When comparing the injected flow rate levels with the acoustically-estimated gas volume released in the form of bubbles, correlation can be observed. First, the increase of gas injection occurring on 17th June from 150 kg d^{-1} (58.6 L/min SATP) to 210 kg d^{-1} (82.1

L/min SATP) produces an increase in gas release from the seafloor as seen in Fig. 11(c) by the dashed black line (increase during 18^{th} of June). This dashed line represents the 24 hour rolling average based on the upper bound of the confidence interval (grey area) of which this tracks intensity changes in flow rates over a day period. From the 15^{th} at 12.00 am to the 17^{th} at 00.00 am, the average flow rate of the upper bound is of 9.2 kg d^{-1} (3.6 L/min SATP) and from the 18^{th} 02.00 pm to the 20^{th} 02.00 am, estimates are of 16.9 kg d^{-1} (6.6 L/min SATP). These two periods of time were chosen because the noise seems to be limited. This gives an increase of 83.2% when including the difference in mean tidal levels. This is a response to a 40% increase in gas injection. Further, the gas injection drops on 21^{st} June and shows direct effect on the gas escape from the seafloor as shown by the sharper decrease at this time in Fig. 11(c). Finally, the estimates level off when the gas injection is stopped, correlating with photographic observations that also showed that the bubble emissions stop shortly after the end of the gas injection.

On 19^{th} June at 11.00 am, diver measurements of each individual bubble stream were performed using an inverse funnel. The gas collection was performed over 49 minutes at high tide and measured 31.8 kg d^{-1} (12.4 L/min SATP) with the mass flow rates from streams spanning 0.1 kg d^{-1} (0.1 L/min SATP) to 2.4 kg d^{-1} (0.9 L/min SATP). This measure is represented by a black cross marker in Fig. 11 and represents 15% of the injected CO_2 at the time. The estimates from the inversion averaged over the measurement period, using $R_{\epsilon 0\text{i}}/R_0 = 2.8 \times 10^{-4}$ (mean value) is 15.9 kg d^{-1} (6.2 L/min SATP), 7.5% of the injected gas. The initial amplitude of bubble wall pulsation for the breathing mode required to match the measurements from the divers is $R_{\epsilon 0\mathrm{i}}/R_0 = 2 \times 10^{-4}$. As explained in Sec. 3 B, on 19$^{\mathrm{th}}$ June at the time of diver measurements (11.00 am to 11.49 am), the inferred gas flow rates from the hydrophone are contaminated by noise. Comparison of the diver-generated flux estimate with the acoustically-inferred fluxes at similar points in the tidal cycle at the same conditions of gas injection rate where the impact of noise is minimized allows refinement of the estimate of flow rate and $R_{\epsilon 0\mathrm{i}}/R_0$. These are computed over four periods. On 19$^{\mathrm{th}}$ June between 11.00 pm and 11.49 pm, averaged flow rate of 6.6 kg d^{-1} (2.6 L/min SATP), $R_{\epsilon 0\mathrm{i}}/R_0 = 1.3 \times 10^{-4}$. On 18$^{\mathrm{th}}$ June between 11.00 pm and 11.49 pm, averaged flow rate of 6.2 kg d^{-1} (2.4 L/min SATP), $R_{\epsilon 0\mathrm{i}}/R_0 = 1.2 \times 10^{-4}$. On 18$^{\mathrm{th}}$ June between 11.00 am and 11.49 am, averaged flow rate of 5.3 kg d^{-1} (2.1 L/min SATP), $R_{\epsilon 0\mathrm{i}}/R_0 = 1.1 \times 10^{-4}$. On 17$^{\mathrm{th}}$ June between 11.00 pm and 11.49 pm, averaged flow rate of 5.3 kg d^{-1} (2.1 L/min SATP), $R_{\epsilon 0\mathrm{i}}/R_0 = 1.1 \times 10^{-4}$. This refines the estimated flow rates at the time of the diver measurements to 5.9 ± 0.7 kg d^{-1} (2.3 ± 0.3 L/min SATP) and the estimation for $R_{\epsilon 0\mathrm{i}}/R_0$ to $R_{\epsilon 0\mathrm{i}}/R_0 = 1.2 \times 10^{-4} \pm 6.8 \times 10^{-6}$.

The quantitative assessments of CO_2 released as free gas (by the divers and using passive acoustics) is only a fraction of the injected CO_2 ($\approx 15\%$) and the remaining ($\approx 85\%$) was retained in the sediments during the limited time of the observation. Although free gas trapped within the sediment layers could be observed using seismic reflection surveying[48], Blackford et al.[26] suggest that a large part of the injected gas was dissolved in sediment pore waters. It is likely that sediments in general can build up reservoirs of free and dissolved gas, both of which may become released from sediments at a later time.

In summary, even when using only a single hydrophone, the passive acoustic technique managed to obtain real time continuous data over 7 days of the gas flux from the QICS experiment, in agreement with the single data point provided by divers who directly collected gas. The source of uncertainty in the acoustically-induced gas flux is well characterized and the route to reducing it is well-understood. Furthermore, the technique also provides real time and continuous monitoring of the bubble size distribution, although space requirements must postpone presentation of this until a later paper. All these features are as predicted by Leighton and White[24].

5 Conclusion

The accuracy of a passive acoustic inversion model for the quantification of gas leaks proposed by Leighton and White[24] is studied and presented in this paper. First, acoustic measurements were performed under laboratory conditions in a large test tank. This allowed calculations of flow rates that were compared to independent direct measurements from a mass flow meter. The results of this study exhibit an agreement at a practically useful level for high flow rates. As expected, at lower flow rates the reduction of SNR decreases the accuracy of the estimate. At low rates it would be better to obtain gas flux estimates from the detection of single bubble signatures. The method explored in this paper is designed for the high gas volume regime where the detection of individual bubble signatures is not feasible. The accuracy of the method is found to rely mostly upon the initial amplitude of bubble wall pulsation for the breathing mode. Using two different types of nozzle for bubble releases, estimates for this quantity are different. However, in both cases, the relative change in flow rate is measured accurately from the acoustic emissions. Using optimized values, the gas volumes that are released are estimated with good accuracy.

Then, in the framework of the QICS project, this technique was deployed at sea and was aimed at quantifying CO_2 gas that was released at different rates. It is observed that the estimates inferred from the acoustic data correlate well with the different changes in flow rates and this gives insight into the gas released in the form of bubbles in response to a change in gas injection. However, the tide is found to have a the most dominant effect on the amount of gas being released. High tide is associated with low gas release and low tide with high gas release. This correlates with photographic observations. A decrease of 15.1 kg d^{-1} (5.9 L/min SATP) in flow rate for each meter of tide increase is estimated. These changes in flow rates are mostly occurring when the tidal cycle is at its local maximum or minimum[60].

A key parameter in the passive inversion model used in this paper (Sec. 2) is the initial amplitude of the bubble wall ($R_{\epsilon 0i}/R_0$) that controls the initial strength of the acoustic emission when a bubble is released. This quantity varies with the type of injection and in this study it is estimated for three types of bubble injections. From the laboratory experiments, it is estimated by comparing acoustically-inferred flow rates to measurements from a mass flow meter and: $R_{\epsilon 0\mathrm{i}}/R_0 = 1.6 \times 10^{-4}$ for the bubbling stone; $R_{\epsilon 0\mathrm{i}}/R_0 = 3.5 \times 10^{-4}$ for the needle array (1 mm inner diameter). From the data collected at sea (gas seeping from the seabed), $R_{\epsilon 0\mathrm{i}}/R_0$ is estimated by comparing acoustically-estimated flow rates with direct measurements from divers and $R_{\epsilon 0\mathrm{i}}/R_0 = 1.2\times 10^{-4} \pm 6.8\times 10^{-6}$. It is perhaps not unexpected for needles to generate a higher initial excitation than either stones or sediments at this flow rate because they concentrate gas emission in both space and time. Consequently, at low flow rate needles give intense clean injections. At higher flow rates, the multiple excitations of each bubble released (as observed by Leighton et al.[21]) are consolidated by spectral methods into an effective single $R_{\epsilon 0\mathrm{i}}/R_0$ that will be several times that of the actual $R_{\epsilon 0\mathrm{i}}/R_0$ that occurs in each component of the multiple emission. In this way the passive acoustic method automatically corrects for the multiple excitations observed by Leighton et al.[21] if the inversion uses the 'effective $R_{\epsilon 0\mathrm{i}}/R_0$' that is appropriate for the type of injector, orifice or substrate through which the gas emerges.

Here, only quantification was of interest because there was prior knowledge of the location of the bubble release. The deployment of the limiting option of a single hydrophone was then not critical for detecting gas leaks because the importance of the detection capability of the system was of low importance. The capability of a single hydrophone to detect gas bubbles is limited because of the impact of background noise. However, as discussed by Leighton and White[24], the use of an array of hydrophones could be beneficial in order to increase SNR and provide the ability to localise the sound emitted by the gas bubbles.

This study is the first to quantify gas fluxes from a large seabed leak using passive emissions. Previous at-sea investigations have used active acoustics to locate gas seeps[15,12,4,63]. It has been shown that quantification can also be performed using such systems[10,14,16,64,65]. For example, using a hull mounted downward looking echosounder, Caudron et al.[10] quantified CO_2 gas emission in the water column using the method by Ostrovsky et al.[14]. However, such measures only constitute snapshots at a specific point in time and do not usually provide coverage of the development of the leak. This can be assessed by long deployment of sonar units[64,65] (e.g. mounted on a lander or an ROV) but the power requirements are significant. In that respect, the use of passive acoustic sensors presents a low cost and low power consumption option as this study shows is useful for monitoring gas releases.

A final point, which suggests the use of both active and passive techniques for cross-validation, is that active and passive acoustical methods for bubble quantification, have differing limitations. The passive acoustic technique is limited by the requirement to know or assume the excitation amplitude of the bubble ($R_{\epsilon 0 \mathrm{i}}/R_0$) and the distance from the bubble to the sensor, and becomes increasingly inaccurate as the signal to noise level falls. The active acoustic technique is prone to the ambiguity between large and resonant bubbles discussed in Sec. 4 C. Furthermore, seeps tend to emit relatively large bubbles compared to the ones measured sometime after an ocean wave has broken, for which active acoustic techniques were originally developed. Consequently the bubble theory used for ocean wave studies[66] may, for high frequencies, become inapplicable for studying seeps because the bubble size is no longer much less than an acoustic wavelength[34,35]. Since the limitations of active and passive acoustic techniques are so different, simultaneous deployment and cross-validation would seem a useful route[23].

Acknowledgments

The studentship of Mr. Bergès is partially sponsored by Statoil Ltd. The authors thank Michal Tomczyk for help with the test tank experiments, Grant Deane and Dale Stokes for making available to us the raw data from figure 7 of reference 33, Dr Trond Erland Bustnes of Statoil for providing guidance on industrial practicalities and requirements, and Jonathan Bull for helpful comments on the manuscript. We thank the crew of research vessel Seol Mara for their assistance and Henrik Stahl and Pete Taylor for overseeing the experiment and general assistance. The QICS experiment was funded by NERC (NE/H013962/1) and the Scottish government. Tidal data were provided by SAMS through the INIS Hydro projet.

REFERENCES

1. T. G. Leighton. *The acoustic bubble.* Academic Press, London, 1994.

2. C. Teal. Subsea leak detection. *Exploration & Production*, 6(1), 2007.

3. Det Norske Veritas. Selection and use of subsea leak detection systems. Technical report, Recommended Practice DNV-RP-F302, 2010.

4. G. K. Westbrook, K. E. Thatcher, E. J. Rohling, A. M. Piotrowski, H. Pälike, A. H. Osborne, E. G. Nisbet, T. a. Minshull, M. Lanoisellé, R. H. James, V. Hühnerbach, D. Green, R. E. Fisher, A. J. Crocker, A. Chabert, C. Bolton, A. Beszczynska-Möller, C. Berndt, and A. Aquilina. Escape of methane gas from the seabed along the West Spitsbergen continental margin. *Geophysical Research Letters*, 36(15):L15608, August 2009.

5. A. G. Judd. The global importance and context of methane escape from the seabed. *Geo-Marine Letters*, 23(3-4):147–154, 2003.

6. D. K. Woolf and S. A. Thorpe. Bubbles and the air-sea exchange of gases in near-saturation conditions. *Journal of Marine Research*, 49(3):435–466, 1991.

7. I. M. Brooks, M. J. Yelland, R. C. Upstill-Goddard, P. D. Nightingale, S. Archer, E. D'Asaro, R. Beale, C. Beattie, B. Blomquist, A. A. Bloom, B. J. Brooks, J. Cluderay, D. Coles, J. Dacey, M. DeGrandpre, J. Dixon, W. M. Drennan, J. Gabriele, L. Goldsen, N. Hardman-Mountford, M. K. Hill, M. Horn, P. Hsueh, B. Huebert, G. de Leeuw, T. G. Leighton, M. Liddicot, J. J. N. Lingard, C. McNeil, J. B. McQuaid, B. I. Moat, G. Moore, C. Neill, S. J. Norris, S. O'Doherty, R. W. Pascal, J. Prytherch, M. Rebozo, E. Sahlee, M. Salter, U. Schuster, I. Skjelvan, H. Slagter, M. H. Smith, P. D. Smith, M. Srokosz, J. A. Stephens, P. K. Taylor, M. Telszewski, R. Walsh, B. Ward, D. K. Woolf, D. Young, and H. Zemmelink.

Physical exchanges at the air-sea interface: UK-SOLAS Field Measurements. *Bulletin of the American Meteorological Society*, 90(5):629–644, May 2009.

8. C. Berndt, T. Feseker, T. Treude, S. Krastel, V. Liebetrau, H. Niemann, V. J. Bertics, I. Dumke, K. Dünnbier, B. Ferré, C. Graves, F. Gross, K. Hissmann, V. Hühnerbach, S. Krause, K. Lieser, J. Schauer, and L. Steinle. Temporal constraints on hydrate-controlled methane seepage off Svalbard. *Science*, 343(6168):284–287, January 2014.

9. J. S. Hornafius, D. Quigley, and B. P. Luyendyk. The world's most spectacular marine hydrocarbon seeps (Coal Oil Point, Santa Barbara Channel, California): Quantification of emissions. *Journal of Geophysical Research-Oceans*, 104(C9):20703–20711, 1999.

10. C. Caudron, A. Mazot, and A. Bernard. Carbon dioxide dynamics in Kelud volcanic lake. *Journal of Geophysical Research*, 117(B5):B05102, May 2012.

11. J. Greinert and B. Nutzel. Hydroacoustic experiments to establish a method for the determination of methane bubble fluxes at cold seeps. *Geo-Marine Letters*, 24(2):75–85, May 2004.

12. J. Schneider von Deimling, J. Greinert, N. R. Chapman, W. Rabbel, and P. Linke. Acoustic imaging of natural gas seepage in the North Sea: Sensing bubbles under control of variable currents. *Limnology and Oceanography: Methods*, 8:155–171, June 2010.

13. I. Ostrovsky. Methane bubbles in Lake Kinneret: Quantification and temporal and spatial heterogeneity. *Limnology and oceanography*, 48(3):1030–1036, 2003.

14. I. Ostrovsky, D. F. Mcginnis, L. Lapidus, and W. Eckert. Quantifying gas ebullition with echosounder: the role of methane transport by bubbles in a medium-sized lake. *Limnology and Oceanography: Methods*, 6:105–118, 2008.

15. A. Nikolovska and J. J. Schanze. Acoustic methane seepage quantification model design, experiments and deep-sea application. In *OCEANS 2007-Europe*, pages 1–6, Aberdeen, 18-21 June 2007. IEEE-Institute of Electrical and Electronic Engineers.

16. N. Shakhova, I. Semiletov, I. Leifer, V. Sergienko, A. Salyuk, D. Kosmach, D. Chernykh, C. Stubbs, D. Nicolsky, V. Tumskoy, and Ö. Gustafsson. Ebullition and storm-induced methane release from the East Siberian Arctic Shelf. *Nature Geoscience*, 7:64–70, November 2014.

17. T. G. Leighton and A. J. Walton. An experimental study of the sound emitted from gas bubbles in a liquid. *European Journal of Physics*, 8:98–104, 1987.

18. C. A. Greene and P. S. Wilson. Laboratory investigation of a passive acoustic method for measurement of underwater gas seep ebullition. *Journal of the Acoustical Society of America*, 131(1):EL61–EL66, 2012.

19. A. Nikolovska and C. Waldmann. Passive acoustic quantification of underwater gas seepage. In *OCEANS 2006*, pages 1–6, Boston, 18-21 Sept. 2006. IEEE-Institute of Electrical and Electronic Engineers.

20. I. Leifer and D. Tang. The acoustic signature of marine seep bubbles. *The Journal of the Acoustical Society of America*, 121(1):EL35–EL40, 2007.

21. T. G. Leighton, K J Fagan, and J E Field. Acoustic and photographic studies of injected bubbles. *European Journal of Physics*, 12:77–85, 1991.

22. T. G. Leighton, P. R. White, and M. F. Schneider. The detection and dimension of bubble entrainment and comminution. *Journal of the Acoustical Society of America*, 103(4):1825–35, 1998.

23. T. G. Leighton, D. G. Ramble, and A. D. Phelps. The detection of tethered and rising bubbles using multiple acoustic techniques. *The Journal of the Acoustical Society of America*, 101(5):2626–2635, May 1997.

24. T. G. Leighton and P. R. White. Quantification of undersea gas leaks from carbon capture and storage facilities, from pipelines and from methane seeps, by their acoustic emissions. *Proceedings of the Royal Society a-Mathematical Physical and Engineering Sciences*, 468(2138):485–510, 2012.

25. J. C. Blackford and J. Kita. A Novel Experimental Release of CO2 in the Marine Environment to Aid Monitoring and Impact Assessment. *Energy Procedia*, 37:3387–3393, 2013.

26. J. Blackford, H. Stahl, J. M. Bull, B. J. P. Bergès, M. Cevatoglu, A. Lichtschlag, D. Connelly, R. H. James, J. Kita, D. Long, M. Naylor, K. Shitashima, D. Smith, P. Taylor, I. Wright, M. Akhurst, B. Chen, T. M. Gernon, C. Hauton, M. Hayashi, H. Kaieda, T. G. Leighton, T. Sato, M. D. J. Sayer, M. Suzumura, K. Tait, M. E. Vardy, P. R. White, and S. Widdicombe. Detection and impacts of leakage from sub-seafloor deep geological carbon dioxide storage. *Nature Climate Change*, 4:1011–1016, September 2014.

27. G. E. Updegraff and V. C. Anderson. Bubble noise and wavelet spills recorded 1 m below the ocean surface. *The Journal of the Acoustical Society of America*, 89(5):2264–2279, 1991.

28. M. R. Loewen and W. K. Melville. A model of the sound generated by breaking waves. *The Journal of the Acoustical Society of America*, 90(4):2075–2080, 1991.

29. H. C. Pumphrey and A. J. Walton. Experimental study of the sound emitted by water drops impacting on a water surface. *European Journal of Physics*, 9(3):225–231, July 1988.

30. H. Medwin and M. M. Beaky. Bubble sources of the Knudsen sea noise spectra. *The Journal of the Acoustical Society of America*, 86(3):1124, September 1989.

31. H. C. Pumphrey and L. A. Crum. Free oscillations of near-surface bubbles as a source of the underwater noise of rain. *The Journal of the Acoustical Society of America*, 87(1):142, January 1990.

32. G. B. Deane and M. D. Stokes. The acoustic signature of bubbles fragmenting in sheared flow. *The Journal of the Acoustical Society of America*, 120(6):EL84, November 2006.

33. G. B. Deane and M. D. Stokes. The acoustic excitation of air bubbles fragmenting in sheared flow. *Journal of the Acoustical Society of America*, 124(6):3450–3463, 2008.

34. M. A. Ainslie and T. G Leighton. Near resonant bubble acoustic cross-section corrections, including examples from oceanography, volcanology, and biomedical ultrasound. *The Journal of the Acoustical Society of America*, 126(5):2163–75, November 2009.

35. M. A. Ainslie and T. G. Leighton. Review of scattering and extinction cross-sections, damping factors, and resonance frequencies of a spherical gas bubble. *Journal of the Acoustical Society of America*, 130(5):3184–3208, 2011.

36. A. Prosperetti. Thermal effects and damping mechanisms in the forced radial oscillations of gas bubbles in liquids. *The Journal of the Acoustical Society of America*, 61(1):17–27, 1977.

37. Y. Zhang and S. C. Li. Notes on radial oscillations of gas bubbles in liquids: thermal effects. *The Journal of the Acoustical Society of America*, 128(5):EL306–EL309, November 2010.

38. P. C. Hansen. *Rank-Deficient and Discrete Ill-Posed Problems: Numerical Aspects of Linear Inversion*. SIAM-Society for Industrial and Applied Mathematics, 1999.

39. P. C. Hansen. *Discrete Inverse Problems: Insight and Algorithms (Fundamentals of Algorithms)*. SIAM-Society for Industrial and Applied Mathematics, 2010.

40. G. B. Deane and H. Czerski. A mechanism stimulating sound production from air bubbles released from a nozzle. *Journal of the Acoustical Society of America*, 123(6):EL126–EL132, 2008.

41. H. Czerski. A candidate mechanism for exciting sound during bubble coalescence. *Journal of the Acoustical Society of America*, 129(3):EL83–EL88, 2011.

42. H. Czerski and G. B. Deane. The effect of coupling on bubble fragmentation acoustics. *Journal of the Acoustical Society of America*, 129(1):74–84, 2011.

43. A. D. Pierce. *Acoustics: an Introduction to Its Physical Principles and Applications.* American Institute of Physics, 1989.

44. R. A. Hazelwood and S. P. Robinson. Underwater acoustic power measurements in reverberant fields. In *OCEANS 2007 - Europe*, pages 1–6, Aberdeen, 18-21 June 2007. IEEE-Institute of Electrical and Electronic Engineers.

45. T. G. Leighton, P. R. White, C. L. Morfey, J. W. L. Clarke, G. J. Heald, H. A. Dumbrell, and K. R. Holland. The effect of reverberation on the damping of bubbles. *Journal of the Acoustical Society of America*, 112(4):1366–1376, 2002.

46. T. G. Leighton, D. G. Ramble, A. D. Phelps, C. L. Morfey, and P. P. Harris. Acoustic detection of gas bubbles in a pipe. *Acta Acustica united with Acustica*, 84(5):801–814, 1998.

47. P. Taylor, H. Stahl, M.E. Vardy, J. M. Bull, M. Akhurst, C. Hauton, R.H. James, A. Lichtschlag, D. Long, D. Aleynik, M. Toberman, M. Naylor, D. Connelly, D. Smith, M. D.J. Sayer, S. Widdicombe, I. C. Wright, and J. Blackford. A novel sub-seabed CO2 release experiment informing monitoring and impact assessment for geological carbon storage. *International Journal of Greenhouse Gas Control*, in press, October 2014.

48. M. Cevatoglu, J. M. Bull, M. E. Vardy, T. M. Gernon, I. C. Wright, and D. Long. Gas migration pathways, controlling mechanisms and changes in sediment physical properties observed in a controlled sub-seabed CO2 release experiment. *International Journal of Greenhouse Gas Control*, (this issue), 2014.

49. J. Gordon and S. Northridge. Potential impacts of Acoustic Deterrent Devices on Scottish Marine Wildlife. Technical report, Scottish Natural Heritage Commissioned Report F01AA404, 2002.

50. T. G. Leighton, P. R. White, and D. C. Finfer. The sounds of seas in space. In *Proceedings of the International Conference on Underwater Acoustic Measurements, Technologies and Results*, pages 833–40, Heraklion, Crete, Greece, 28 June-1 July 2005.

51. T. G. Leighton and G. B. N. Robb. Preliminary mapping of void fractions and sound speeds in gassy marine sediments from subbottom profiles. *Journal of the Acoustical Society of America*, 124(5):EL313–EL320, 2008.

52. T. G. Leighton. A method for estimating sound speed and the void fraction of bubbles from sub-bottom sonar images of gassy seabeds. *ISVR technical report*, 320:1–21, December 2007.

53. T. G. Leighton. Theory for acoustic propagation in marine sediment containing gas bubbles which may pulsate in a non-stationary nonlinear manner. *Geophys. Res. Lett.*, 34(17):L17607, 2007.

54. I. Leifer and J. Boles. Turbine tent measurements of marine hydrocarbon seeps on subhourly timescales. *Journal of Geophysical Research*, 110(C1):C01006, 2005.

55. I. Leifer and J. Boles. Measurement of marine hydrocarbon seep flow through fractured rock and unconsolidated sediment. *Marine and Petroleum Geology*, 22(4):551–568, April 2005.

56. M. E. Torres, J. McManus, D. E. Hammond, M. A. de Angelis, K. U. Heeschen, S. L. Colbert, M. D. Tryon, K. M. Brown, and E. Suess. Fluid and chemical fluxes in and out of sediments hosting methane hydrate deposits on Hydrate Ridge, OR, I: Hydrological provinces. *Earth and Planetary Science Letters*, 201(3-4):525–540, August 2002.

57. K. U. Heeschen, R. W. Collier, M. A. de Angelis, P. Linke, E. Suess, and G. P. Klinkhammer. Methane sources, distributions, and fluxes from cold vent sites at Hydrate Ridge, Cascadia Margin. *Global Biogeochemical Cycles*, 19(2):GB2016, July 2005.

58. K. U. Heeschen, A. M. Trehu, R. W. Collier, E. Suess, and G. Rehder. Distribution and height of methane bubble plumes on the Cascadia Margin characterized by acoustic imaging. *Geophysical Research Letters*, 30(12):1643, June 2003.

59. S. Hsu, S. Wang, Y. Liao, T. F. Yang, S. Jan, J. Lin, and S. Chen. Tide-modulated gas emissions and tremors off SW Taiwan. *Earth and Planetary Science Letters*, 369-370:98–107, May 2013.

60. J. R. Boles, J. F. Clark, I. Leifer, and L. Washburn. Temporal variation in natural methane seep rate due to tides, Coal Oil Point area, California. *Journal of Geophysical Research*, 106(C11):27077, 2001.

61. T. G. Leighton, S. D. Meers, and P. R. White. Propagation through nonlinear time-dependent bubble clouds and the estimation of bubble populations from measured acoustic characteristics. *Proceedings of the Royal Society of London. Series A: Mathematical, Physical and Engineering Sciences*, 460(2049):2521–2550, 2004.

62. A. D. Phelps and T. G. Leighton. Oceanic bubble population measurements using a buoy-deployed combination frequency technique. *IEEE Journal of Oceanic Engineering*, 23(4):400–10, 1998.

63. A. Nikolovska, H. Sahling, and G. Bohrmann. Hydroacoustic methodology for detection, localization, and quantification of gas bubbles rising from the seafloor at gas seeps from the eastern Black Sea. *Geochemistry Geophysics Geosystems*, 9(10):1–13, October 2008.

64. I. Leblond, C. Scalabrin, and L. Berger. Acoustic monitoring of gas emissions from the seafloor. Part I: quantifying the volumetric flow of bubbles. *Marine Geophysical Research*, 35(3):191–210, June 2014.

65. G. Bayrakci, C. Scalabrin, S. Dupré, I. Leblond, J. Tary, N. Lanteri, J. Augustin, L. Berger, E. Cros, A. Ogor, C. Tsabaris, M. Lescanne, and L. Géli. Acoustic monitoring of gas emissions from the seafloor. Part II: a case study from the Sea of Marmara. *Marine Geophysical Research*, 35(3):211–229, June 2014.

66. S. Vagle and D. M. Farmer. The Measurement of Bubble-Size Distributions by Acoustical Backscatter. *Journal of Atmospheric and Oceanic Technology*, 9(5):630–644, 1992.

Regime	Metered (kg d^{-1})	Needle array (kg d^{-1})	Best fit $R_{\epsilon 0\mathrm{i}}/R_0(-)$ for needle array	Bubbling stone (kg d^{-1})	Best fit $R_{\epsilon 0\mathrm{i}}/R_0(-)$ for bubbling stone
15	3.01	14.68, 0.89	3.02×10^{-4}	5.46, 0.33	1.85×10^{-4}
14	2.79	11.98, 0.72	2.83×10^{-4}	4.6, 0.28	1.76×10^{-4}
13	2.58	10.28, 0.62	2.74×10^{-4}	4.18, 0.25	1.74×10^{-4}
12	2.36	8.9, 0.54	2.66×10^{-4}	3.11, 0.19	1.57×10^{-4}
11	2.15	7.66, 0.46	2.59×10^{-4}	2.64, 0.16	1.52×10^{-4}
10	1.93	6.23, 0.38	2.46×10^{-4}	2.71, 0.16	1.62×10^{-4}
9	1.72	3.67, 0.22	2×10^{-4}	2.34, 0.14	1.59×10^{-4}
8	1.5	4.17, 0.25	2.28×10^{-4}	1.68, 0.10	1.45×10^{-4}
7	1.29	3.14, 0.19	2.14×10^{-4}	1.51, 0.09	1.48×10^{-4}
6	1.07	3.86, 0.23	2.59×10^{-4}	1.6, 0.10	1.67×10^{-4}
5	0.86	4.95, 0.3	3.29×10^{-4}	1.57, 0.09	1.85×10^{-4}
4	0.64	4.71, 0.28	3.7×10^{-4}	1.72, 0.10	2.24×10^{-4}
3	0.43	2.98, 0.18	3.61×10^{-4}	1.85, 0.11	2.84×10^{-4}
2	0.22	2.97, 0.18	5.09×10^{-4}	1.21, 0.07	3.25×10^{-4}
1	0.11	1.29, 0.08	4.75×10^{-4}	0.03, 0.003	0.92×10^{-4}

Table 1: Summary of results from the experiment described in Sec. 3 A for steady flow rates, using the 75th and 25th percentiles from statistical analysis of measured values of $R_{\epsilon 0\mathrm{i}}/R_0$ by Deane and Stokes[33] (Sec. 3 A, $R_{\epsilon 0\mathrm{i}}/R_0 = 1.4 \times 10^{-4}$ and $R_{\epsilon 0\mathrm{i}}/R_0 = 5.6 \times 10^{-4}$). If instead the appropriate value of $R_{\epsilon 0\mathrm{i}}/R_0$ to use for this type of injection is inferred by finding the value that allows the acoustically-inferred gas flux to equal the metered flow, then that enables calculation of best fit values of $R_{\epsilon 0\mathrm{i}}/R_0$, which are shown in the table.

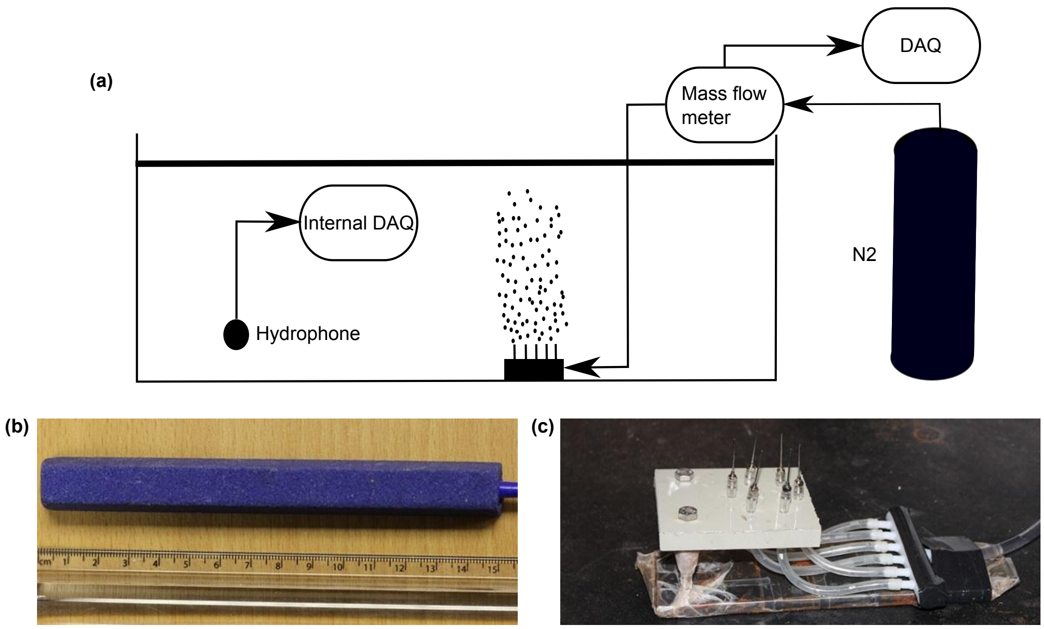

Fig. 1: (Colour) (a): schematic of the experimental set up. Acoustic emissions of gas bubbles were recorded using a calibrated hydrophone with an internal data acquisition unit. Bubbles were released using a nitrogen gas bottle and the bubble generation systems: a bubbling stone (b) and an array of needles (c). The flow rates were acquired using a mass flow meter.

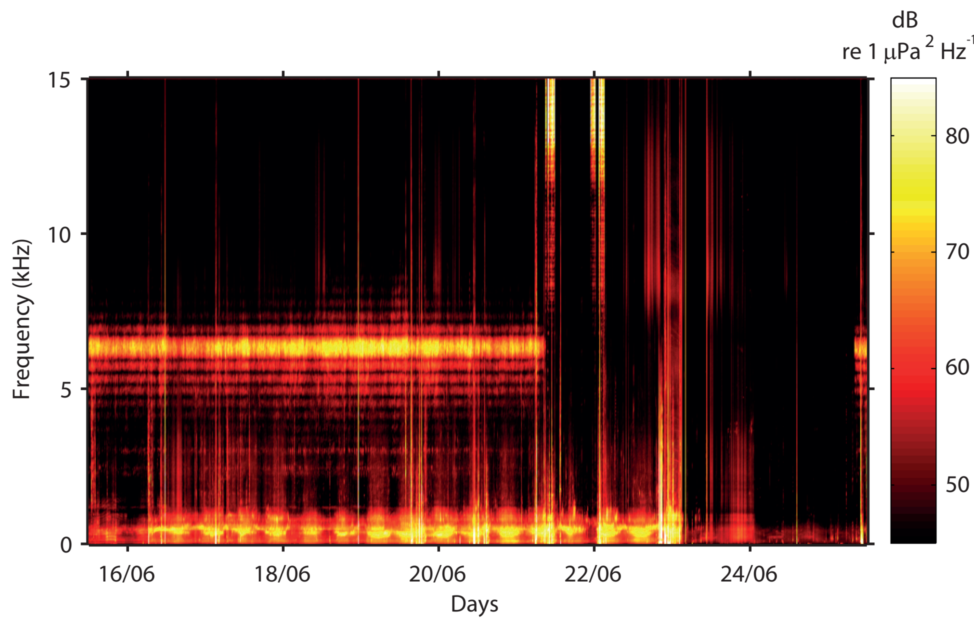

Fig. 2: (Colour) Spectrogram of acoustic signal measured between 15th and 26th June 2012. The gas is stopped being injected on the 22nd 05.07 pm. Seal deterrent device (sdd) signals from fish farms near the experiment site can be observed (Sec. 3 B) with high acoustic energy around the 10 kHz mark. From the 20th 12.00 am to the 25th 12.00 am, the devices were switched off.

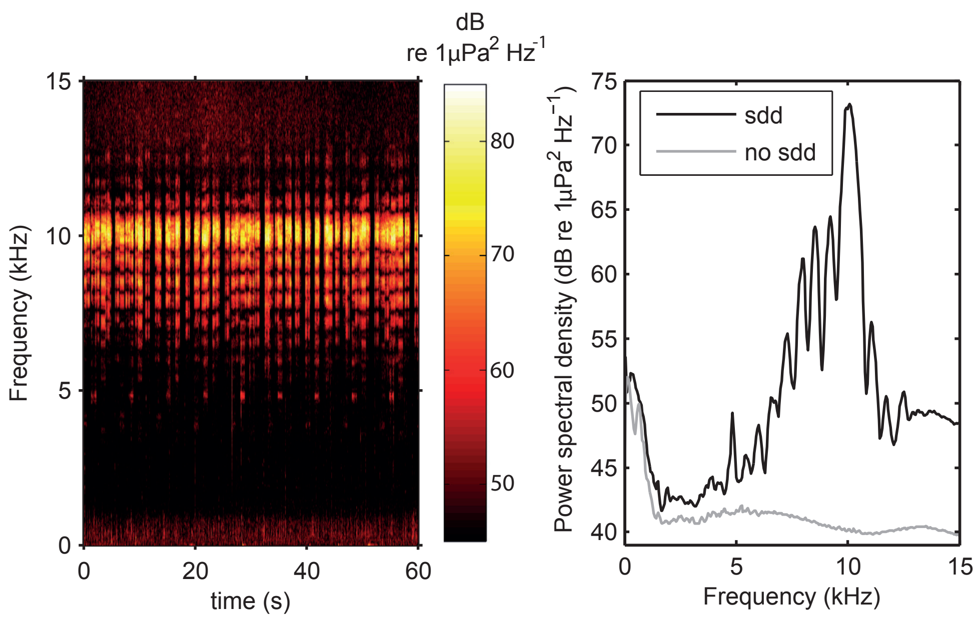

Fig. 3: (Colour) Impact of seal deterrent devices (sdd) used by fish farms that corrupted the collection of acoustic data during the release phase of the QICS project. (a): Spectrogram for a duration of 60 seconds on 25th June (gas injection stopped, no acoustic emission from gas bubbles). (b): Spectrum comparison of signal corrupted by seal deterrent (solid black line) devices with a clean signal (solid grey line).

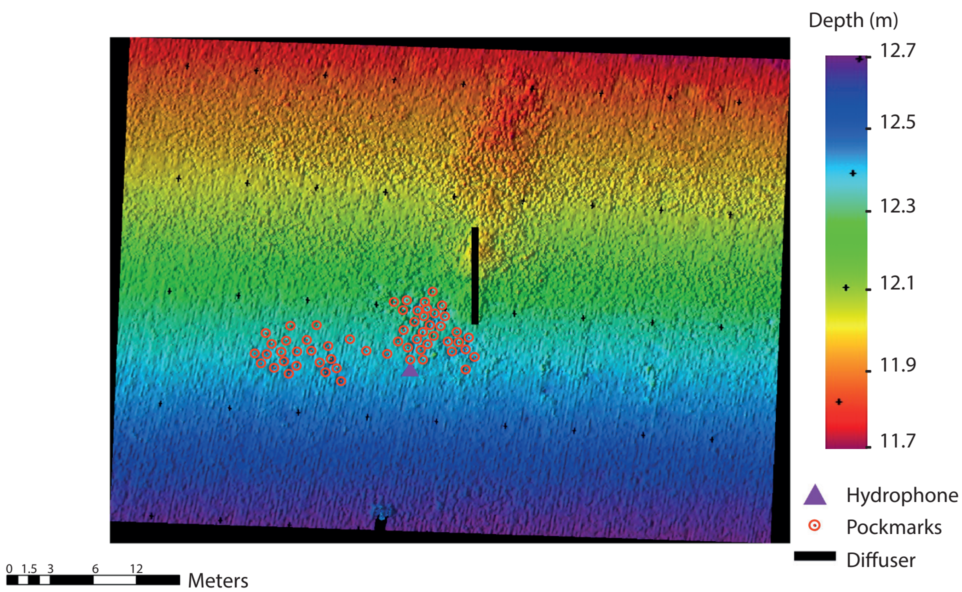

Fig. 4: (Colour) Map of the QICS site showing position of the hydrophone relative to the 5 m long gas diffuser (black line) located 11 m beneath the seabed. The multibeam bathymetry image has been interpreted to show the position of seabed pock marks (white circles) which were the locations of CO_2 bubble streams recorded by the hydrophone (pink triangle). Water depths across the QICS site varied between 10 and 12 m depending on the tidal state.

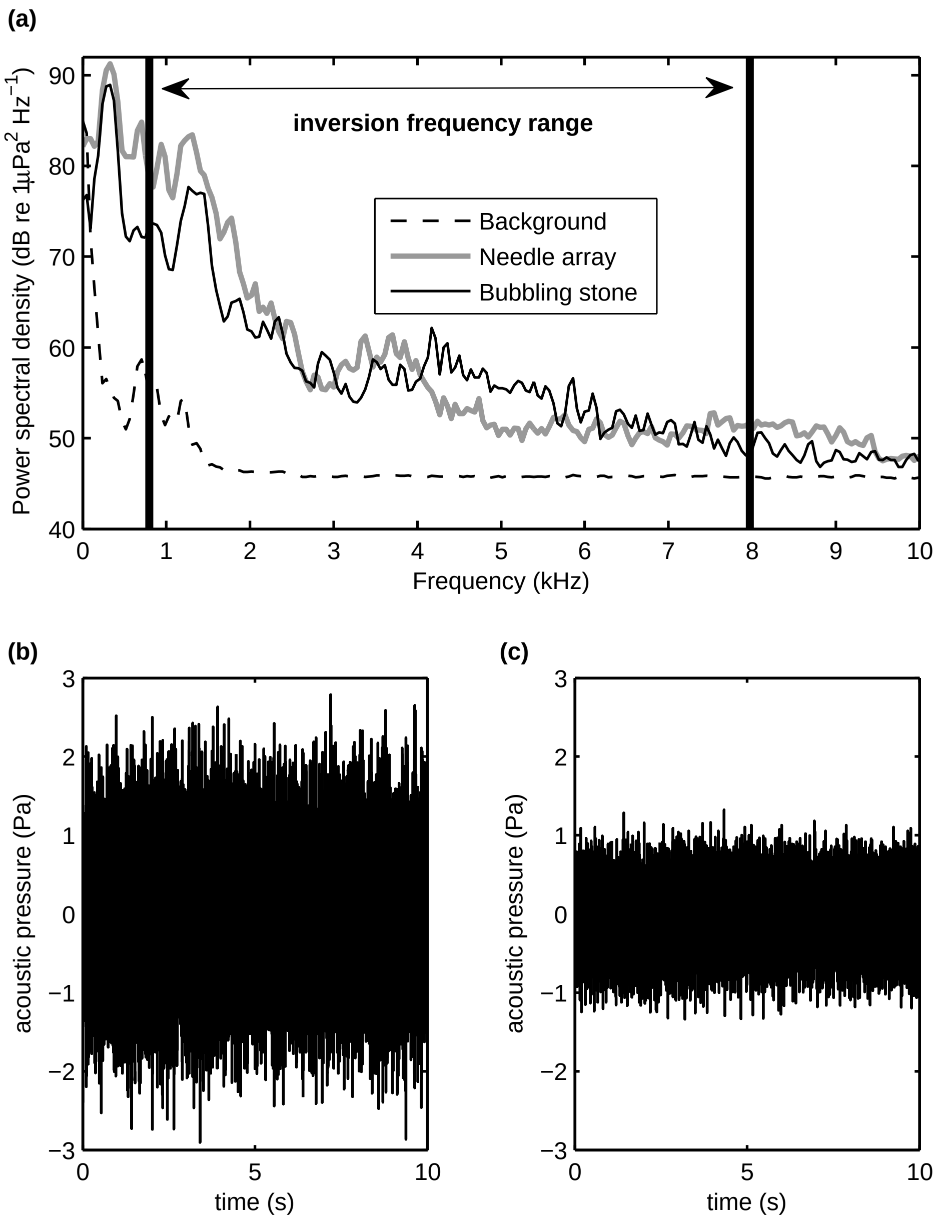

Fig. 5: (a): comparison of spectrum in a frequency band including the one used for the calculations (0.8 kHz to 7.9 kHz) for ambient noise (dashed black line) and signals emitted from the needles array (thick solid grey line) and the bubbling stone (solid black line). The flow rate for these measurements was of 3 kg d^{-1} (regime 15, equivalent to 3.7 L/min SATP). (b): 10 seconds of the signal emitted by the bubble plume generated with the needle array at a flow rate of 3 kg d^{-1} (regime 15, equivalent to 3.7 L/min SATP). The rms level of the signal is of 116.2 dB re 1 μPa. (c): 10 seconds of the signal emitted by the bubble plume generated with the needle array at a flow rate of 0.2 kg d^{-1} (regime 2, equivalent to 0.3 L/min SATP). The rms level of the signal is of 108.2 dB re 1 μPa.

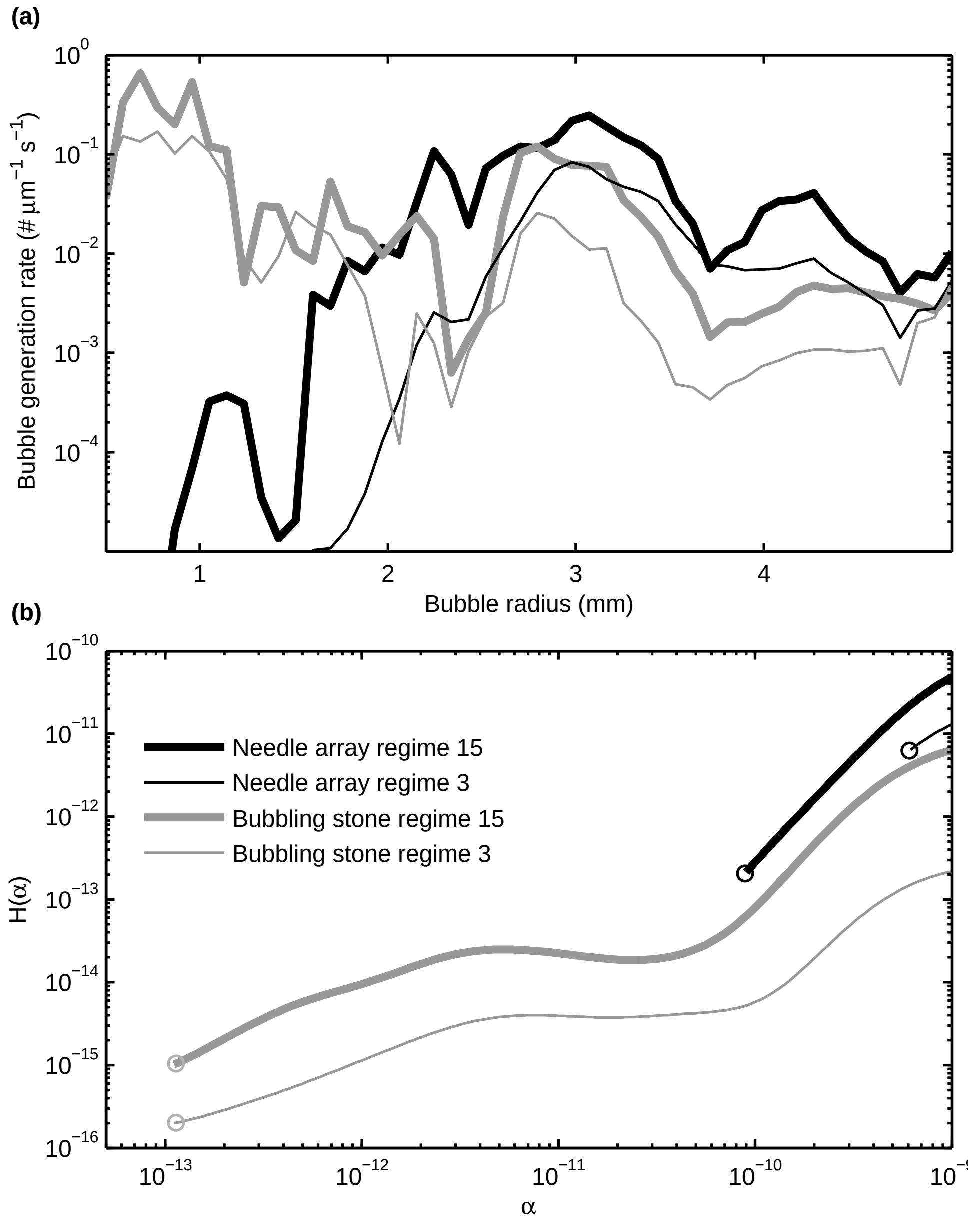

Fig. 6: (a): Plot of the bubble generation rates Ψ obtained from the inversion of the acoustic emission versus bubble radius. (b): GCV functions $H(\alpha)$ used for the determination of the regularization factor α. In both graphs, the results from the needle array is plotted at regime 15 (thick solid black line) and 3 (thin solid black line). At the same regimes, results from the bubbling stone are represented by the thick solid grey line (regime 15) and the thin solid grey line (regime 3). The circle markers are the points corresponding to the values of α used for the inversion.

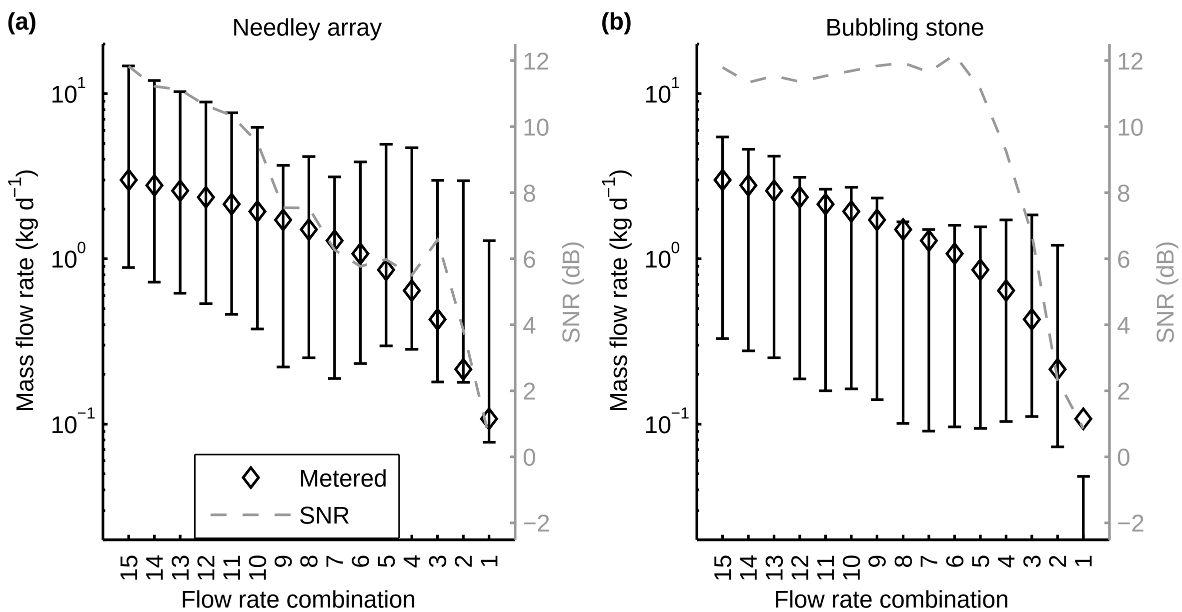

Fig. 7: Comparison of different steady flow rates (left axis) inferred from acoustics (solid black line error bars) and direct flow rate measurements (diamond markers) at different regimes. SNR levels of acoustic signals monitored are also presented (right vertical axis, dashed grey lines). The error bars represent the uncertainty from $R_{\epsilon 0i}/R_0$, calculated using the 75th and 25th percentiles from statistical analysis of measured values by Deane and Stokes[33] (Sec. 3 A, $R_{\epsilon 0i}/R_0 = 1.4 \times 10^{-4}$ and $R_{\epsilon 0i}/R_0 = 5.6 \times 10^{-4}$). (a): needle array. (b): bubbling stone.

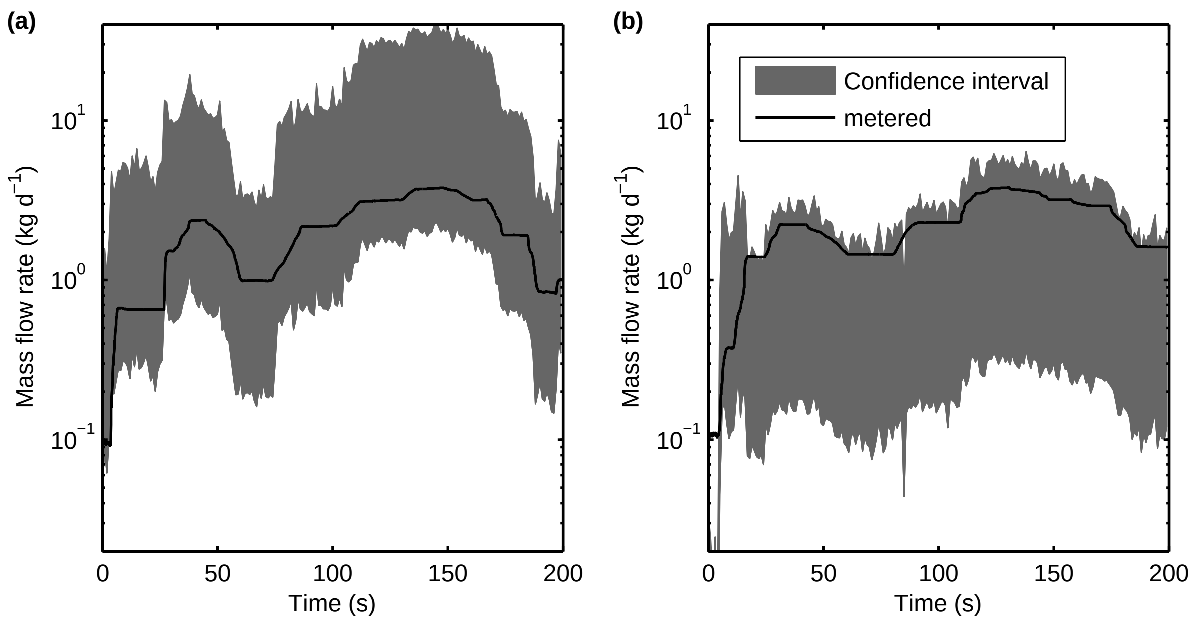

Fig. 8: Comparison between metered (solid black line) and estimates inferred from acoustics (grey area) of fluctuant gas release over 200 seconds. The confidence interval represents the uncertainty on $R_{\epsilon 0 \mathrm{i}}/R_0$. (a): needle array. (b): bubbling stone.

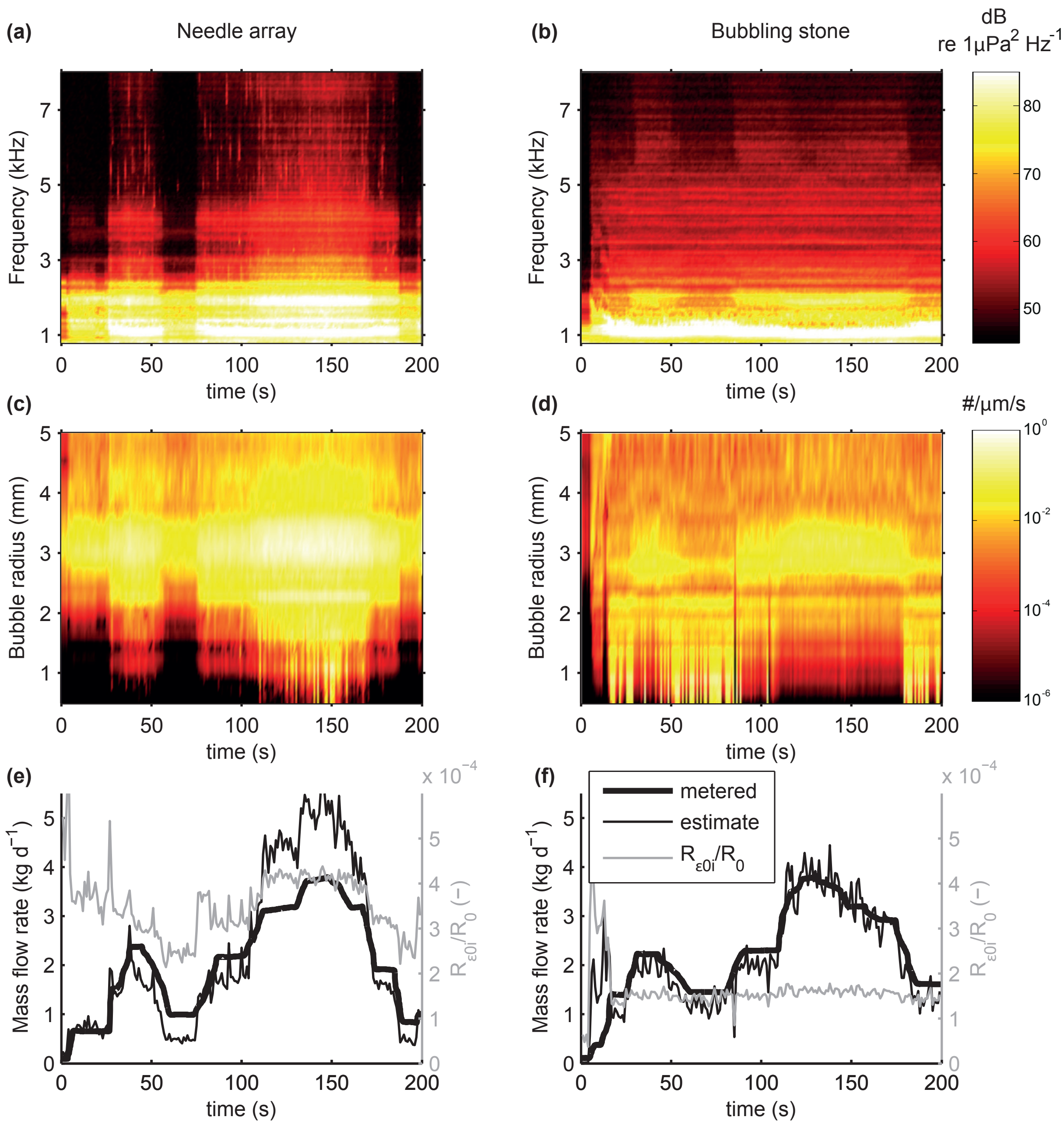

Fig. 9: (Colour) Passive acoustic inversion calculation steps in the case of gas release varying over 200 seconds. Results are given for injected gas using the needle array (graphs on the left) and the bubbling stone (graphs on the right). (a) and (b): spectrogram from the bubble emissions. (c) and (d): resulting bubble generation rates Ψ from the inversion. (e) and (d): mass flow rates and corresponding $R_{\epsilon 0\mathrm{i}}/R_0$. The left axis relate to the mass flow rates that are metered (solid thick black line) and estimated from acoustics (solid thin black line) with an optimized $R_{\epsilon 0\mathrm{i}}/R_0$. The right axis are for the quantities $R_{\epsilon 0\mathrm{i}}/R_0$ that would be required to have mass flow rate measurements matching the direct measurements.

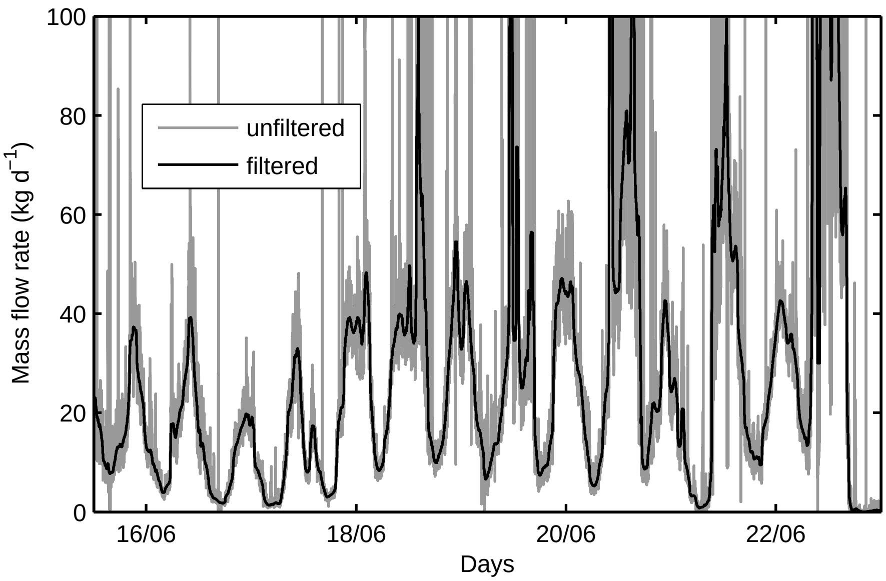

Fig. 10: Mass flow rates estimated from acoustic measurements during the release phase of the QICS project with (solid black line) and without (solid grey line) the application of a 1 hour median filter.

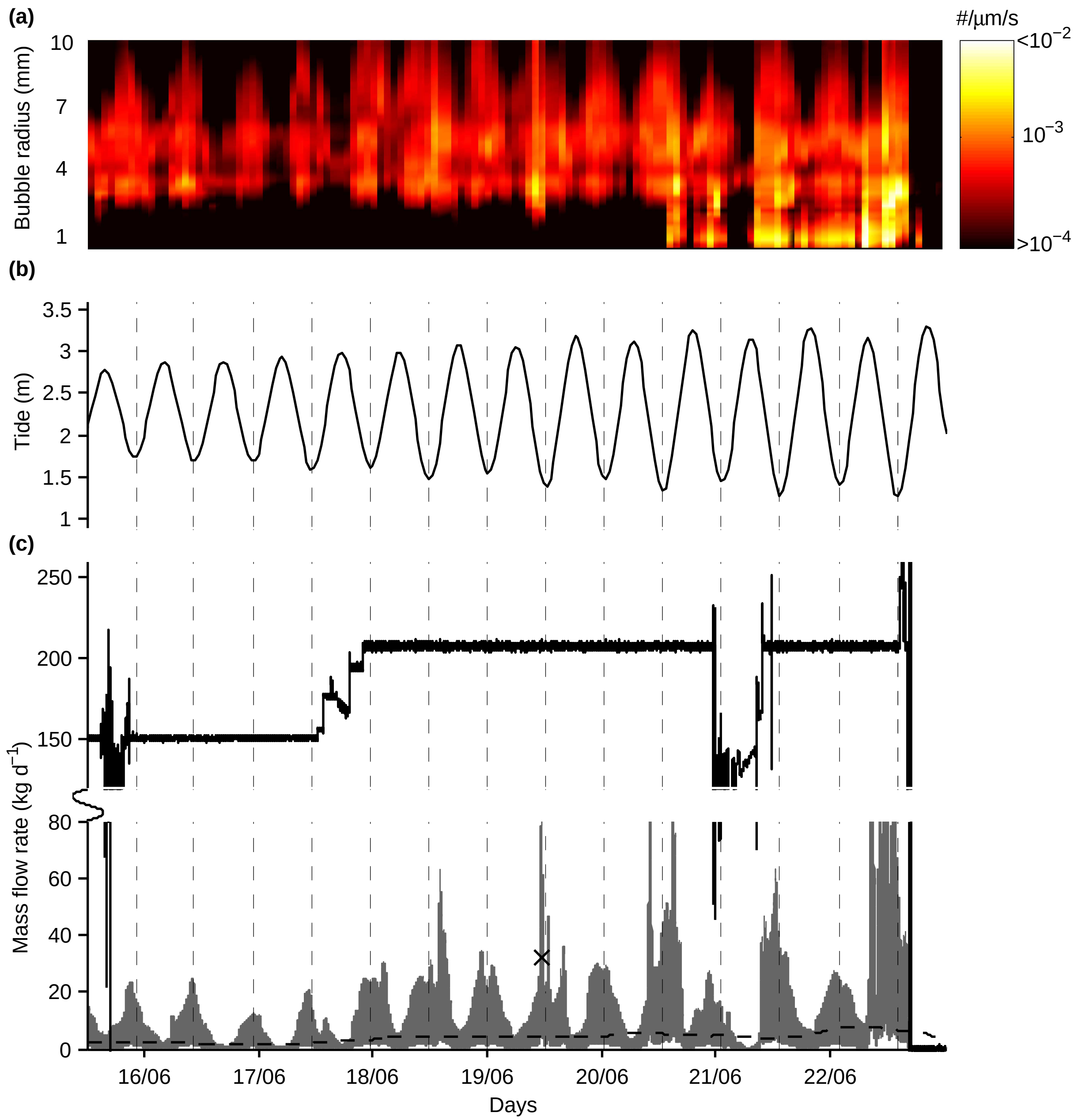

Fig. 11: (Colour) Various results from the release phase of the QICS project. (a): Bubble generation rate Ψ versus days. (b): Tide versus days. (c): injected (solid black line) and acoustically inferred mass flow rates. The acoustic estimates are computed as a confidence interval (grey area) based on uncertainties on $R_{\epsilon 0i}/R_0$ from the 25th and 75th percentiles of the data from Deane and Stokes[33] (Sec. 3 A). The black cross marker represents the diver flow rate measurements on each individual streams. The dashed black line is the 1h moving averaged gas flow rate acoustic estimate showing the general increase after 18th June.

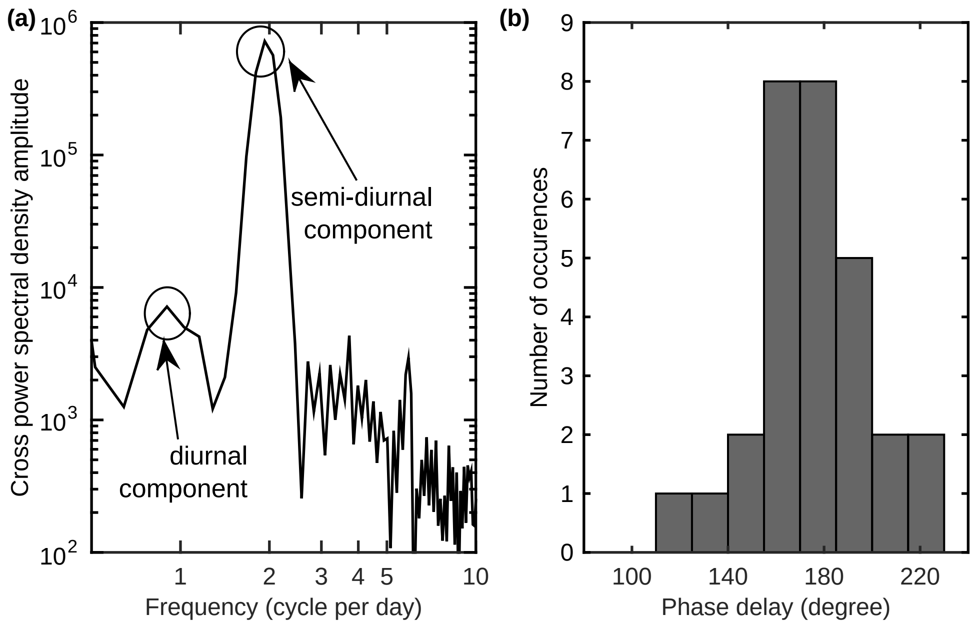

Fig. 12: Correlation between tidal height (Fig. 11(b)) and flow rates inferred from passive acoustics (Fig. 11(c), grey area). (a): Cross power spectral density amplitude versus frequency in cycles per day. The cross power spectral density is computed using a 12 hours Hamming window with 50% overlap. The graph shows high correlation at the semi-diurnal component (≈ 12 hours cycle). A peak is also noticeable at diurnal components (≈ 24 hours cycle). (b): Distribution of phase delay between tidal heights and flow rate estimates for the semi-diurnal component. This gives a phase estimate of 174.8° ± 23° (5.8 ± 0.8 hours).

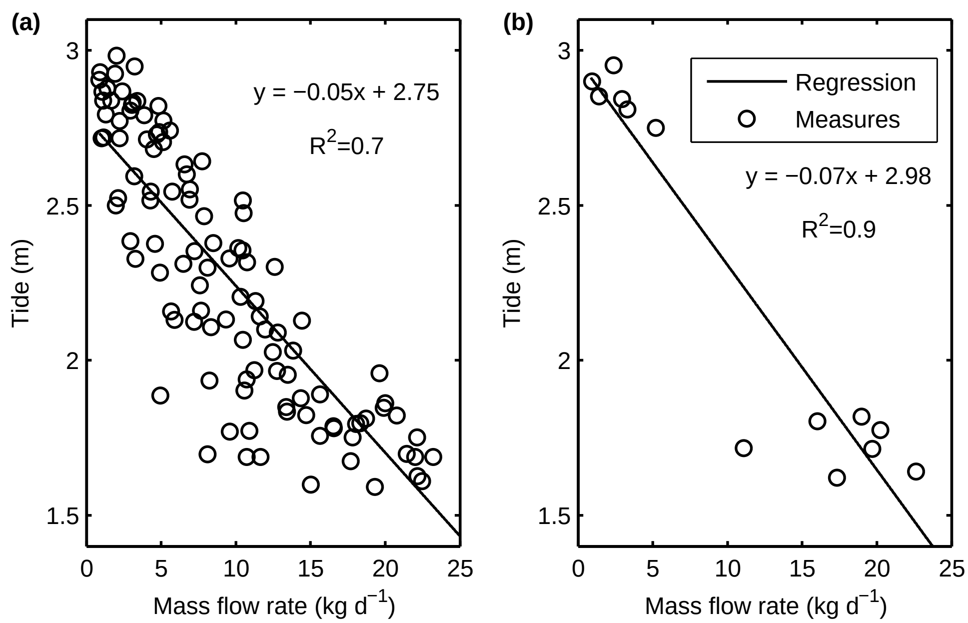

Fig. 13: Tidal levels against mass flow rates inferred from acoustics (from 14th 05:30 pm to 18th 02.00 pm). The circle markers are the flow rate measurements from bubble acoustic emissions. The solid black line is the linear regression of the data points. (a): data points averaged over 43 minutes periods. (b): data points averaged over 86 minutes periods around tide peaks and dips.

List of Figures

List of Tables